UNIVERSITY OF COPENHAGEN

Niels Bohr Institute

Exploring Stellar Clusters as Galactic Sources of High Energy Neutrinos

MSc Thesis

Youyou Li

Supervisor: Markus Ahlers and Enrico Peretti

June 2022

ABSTRACT

Stellar clusters are promising candidates of PeV-atrons (PeV accelerators) in our Galaxy. Diffusive shock acceleration is expected to be efficiently at work at the wind termination shock of these unique objects. Molecular clouds and clumps in the vicinity of the clusters can provide enough target material for a relevant production of hadronic secondaries. Indeed, recent observations by HAWC, Tibet-ASgamma, and LHAASO have identified 0.1-1 PeV gamma-ray emission coincident with nearby stellar clusters such as the Cygnus Cocoon or Westerlund 1 and 2. In this project, we will investigate high-energy gamma-ray and neutrino emission from Galactic stellar clusters. We will model hadronic emission of individual sources and compare our predictions to multimessenger observations. In particular, we investigate the prospects of neutrino telescopes to identify high-energy neutrino emission from stellar clusters.

CONTENTS

1 INTRODUCTION 1

2 COSMIC RAY AND MULTIMESSENGER RELATIONS 3

2.1 CR spectrum . . . 3

2.2 Galactic PeV-atrons . . . 5

2.2.1 The SNR Paradigm . . . 5

2.2.2 CRs from Star Clusters . . . 6

2.3 Propagation of Cosmic Rays . . . 6

2.4 Multi-messenger Investigation . . . 8

2.4.1 Process of Secondary Gamma-ray and Neutrino Production . . . 8

2.4.2 Observational aspects of CR, gamma-ray and neutrino . . . 9

3 TRANSPORT EQUATION AND DIFFUSIVE SHOCK ACCELERATION 12

3.1 CR Diffusion . . . 12

3.2 The Mechanism of DSA . . . 13

3.3 Transport Equation and DSA . . . 16

3.3.1 Example 1: Infinite planar shock . . . 17

3.3.2 Example 2: Planar shock with a Free Escape Boundary . . . 19

4 COSMIC RAY ACCELERATION AT STAR CLUSTERS 23

4.1 Star Cluster Bubble Structure . . . 23

4.2 Star Cluster Profiles . . . 25

4.3 Solution of scenario A . . . 28

4.3.1 Upstream Region . . . 28

4.3.2 Downstream Region . . . 29

4.3.3 Shock Surface . . . 30

4.3.4 Iterative Solution . . . 31

4.4 Solution of Scenario B . . . 32

4.5 Results . . . 34

4.5.1 Scenario A . . . 34

4.5.2 Scenario B . . . 36

5 MULTIMESSENGER INVESTIGATION 39

5.1 Prediction of Neutrino Production at Source . . . 39

5.1.1 The Target Material at Star Clusters . . . 39

5.1.2 Estimation Methods . . . 41

5.1.3 Result: Scenario A . . . 43

5.1.4 Result: Scenario B . . . 45

5.2 Gamma-ray and Neutrino Flux At Earth . . . 46

5.2.1 Neutrino Flavor Oscillation 46
5.2.2 Result and discussion 48
6 CONCLUSION AND OUTLOOK 53
Bibliography 55

1

INTRODUCTION

The measurements carried out by Victor Hess of charged particles in the Earth's atmosphere with balloon flights in 1912 led to the introduction of a new type of cosmic messenger: Cosmic rays (CRs) [1]. CRs are charged particles of astrophysical origin traveling at relativistic velocities and they are observed to span an energy range from MeV (10^6 eV) to more than hundreds of EeV (10^{18} eV) energies. However, there are many puzzles associated with the properties of the observed CR spectrum and the origin of CRs. At the energy of the ~ 4 PeV (4×10^{15} eV), the observed CR spectrum exhibit a change in its power-law index from -2.7 to -3.1, which is called the 'knee' [2]. CRs with energies up to the 'knee' are believed to have Galactic origins. However, the Galactic sources of these CRs are unknown. The challenge of probing CR sources through observations arises from the diffusive behavior when CRs are deflected by magnetic fields on their path from source to Earth. Luckily, the interaction of high energy CRs with their surrounding protons allows one to associate CRs with gamma-rays and neutrino emissions, which can be utilized as messengers to probe CRs in the astronomical environment.

Astrophysical shocks are promising acceleration sites of CRs. The most recognized example is CR acceleration at Supernovae (SNe) and supernova remnants (SNRs) (e.g. [3–5]). However, a series of theoretical works and gamma-ray observations suggest that SNRs could not be able to accelerate particles up to PeV [6–8]. Thus, alternative sources are under investigation. Bubbles inflated by strong winds from star clusters have been proposed to be a possible alternative candidate [9, 10]. The stellar wind converts part of its kinetic energy to CRs through the acceleration process. The energy budget of the stellar wind inferred from gamma-ray observation suggests that PeV energy of CRs can be reached [11]. Studies of the observed gamma-ray spectra and morphology of compact star clusters, such as Westerlund 1 & 2 [12–14], Cygnus Cocoon [15, 16] and NGC3603 [17] support the scenario of CR acceleration at star clusters [8, 18].

In this project, we aim to explore the multimessenger signals of CRs accelerated in young massive star cluster wind bubbles. We will model the gamma-ray and neutrino emissions from hadronic processes when CRs interact with the surrounding protons at the source, and the corresponding fluxes expected at Earth. Two models will be investigated: Model A) focuses

solely on the physical significance of the wind bubble itself in terms of CR acceleration and secondary emissions; Model B) considers also the swept-up interstellar medium (ISM) matter by the wind bubble and its ambient ISM. With these two setups, we can study the impact of the ISM on CR acceleration in a wind bubble, and the contribution to the gamma-ray and neutrino emissions from the interior and exterior regions of the wind bubble. Since gamma-rays have already been observed from regions that coincide with the nearby star clusters, we will apply the models to specific sources: Westerlund 2, and the star-forming region Cygnus Cocoon where the star cluster Cygnus OB2 resides. The expected gamma-ray flux from these sources based on our models will be compared with the observational data. The expected neutrino flux will be evaluated for potential neutrino source detection by the IceCube neutrino observatory in the future.

The thesis is structured as follows: In Chapter 2, we introduce the properties of CRs, and the relation of CRs to other messengers; in Chapter 3, the mechanism of diffusive shock acceleration will be introduced and discussed with examples; in Chapter 4, we apply the diffusive shock acceleration to a young massive star cluster wind bubble, two setups of the model will be calculated and compared; Chapter 4 is devoted to the multimessenger investigation regarding CRs from star clusters. We examine the model of star cluster by comparing expected gamma-ray flux from Cygnus Cocoon and Westerlund 2 with observational data and discuss the observational aspects of the corresponding neutrino flux by IceCube.

2

COSMIC RAY AND MULTIMESSENGER RELATIONS

In the following sections, we focus on general properties of the origin of CRs and how they can be probed with hadronic secondary products. In Section 2.1, we introduce the observed CR all particle spectrum, which leads to the discussion in Section 2.2 on the possible candidates of Galactic PeV-atrons to accelerate Galactic PeV CRs; Section 2.3 focuses on the diffusive property of CR propagation, which brings challenges to extract information of their sources from CR detection; finally, we will discuss the multimessenger approach to investigate CRs in Section 2.4.

2.1 CR SPECTRUM

Cosmic rays are primarily composed of protons, which contribute to $\sim$ 87% of the CR population. The elementary abundance is followed by helium nuclei ($\sim$12%), while heavier atomic nuclei, electrons, and positrons contributes to the remaining 1% [19]. The all-particle CR spectrum observed at Earth by different experiments is shown in Fig.1. It is a steeply falling spectrum that follows roughly a power-law distribution $N(E)dE \propto E^{-\gamma}dE$. The spectrum departs from a power-law distribution at energies less than $\sim$ 30 GeV due to the 'solar potential', namely due to the magnetized solar wind repelling these low-energy particles when propagating to the Earth [20]. At energies of about 4×10^{15} eV (4 PeV) and 3×10^{18} eV (3 EeV), the spectrum experiences changes in the slope of the power-law, and they are called the 'knee' and the 'ankle' respectively [21, 22]. At the 'knee', the power-law index γ changes from $\sim$ 2.7 to $\sim$ 3.1 [2]. The flux of CRs around the 'knee' energy at Earth is 1 $m^{-2}yr^{-1}$. After the 'ankle', the spectrum hardens to a power-law index of $\sim$ 2.6 [22], and the flux drops to 1 $km^{-2}yr^{-1}$.

The nature and sources responsible for the 'knee' and the 'ankle' are matter of active debate in the scientific community [24–28]. There is however a general consensus on the role of supernova remnants in powering the bulk of CRs [29–33]. Experiments carried out by KASCADE and EAS-TOP on measuring the CR energy spectrum by individual elements and groups of elements provided precious insights into understanding the 'knee' [34, 35]. The spectra measured for proton, helium, and iron seem to follow power-laws and have cut-offs at high energies. The energies of the cut-offs are proportional to the nuclear charge

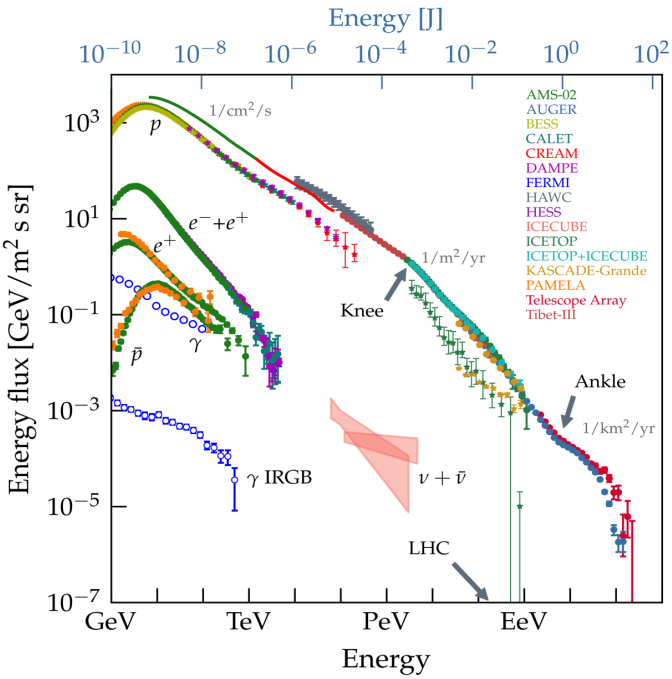

Figure 1: The all-particle CR spectrum as a function of E (energy per nucleon), and its comparison with electron positron, gamma-ray and neutrino observed spectra (image credit: Carmelo Evoli [23]).

Z: $E_{cut} = Z \times 4.5$ PeV [2]. It is an indication that the 'knee' could be a superposition of the cut-off energies of different elements accelerated together by PeV-atrons with rigidity ($R = E/Z$) dependence [36].

The 'ankle' is believed to be the transition from Galactic to extra-galactic species [37, 38]. This is supported by the confinement strength of CRs determined by the combination of the Galactic magnetic field and size. As charged particles, CRs gyrate around magnetic field lines. The radius of such motion is the Larmor radius:

$$R_L = \frac{pc}{qB}, \tag{1}$$

where p is the momentum of the CR particle, c is the speed of light, q is the charge of the particle, and B is the magnetic field. With a mean average magnetic field of $\sim$1 μG [39], a proton with an energy of 3×10^{18} eV has a Larmor radius of $\sim$ 3.2 kpc, which is comparable with the thickness of the magnetized galactic halo [40, 41]. Therefore CRs with energies beyond the 'ankle' can not be confined in our Galaxy. Moreover, the hardening of the spectrum at the ankle to a power-law index of 2.6 suggests that there is a new component of CRs. The correlation of the arrival directions of the highest energy CRs with the large-scale matter distribution in the Universe provided further support to the extra-galactic origin of these CRs [42].

2.2 GALACTIC PEV-ATRONS

The transition of CR components to heavier elements around the 'knee' energy leads to the idea that these CRs are accelerated together in our Galaxy by PeV-atrons. Since the first suggestion made by Baade & Zwicky (1934), Supernova remnant (SNR) has so far been the most recognized source for Galactic cosmic rays (GCRs). In the following subsections, we will first talk about the evidence and challenges of SNRs as Galactic PeV-atrons in subsection 2.2.1; the motivation for suggesting star clusters as PeV-atron candidates will be introduced in subsection 2.2.2.

2.2.1 *The SNR Paradigm*

SNR became the most recognized candidate source of GCRs for several reasons. The leading reason is that SNe are known sources with large energy budget. The predicted CR energy density from the energy released by SNe is consistent with the measured value [3–5, 37]. A typical kinetic energy release of a SN is around $E_{SN} = 10^{51}$ erg [43]. This energy has a weak dependence on whether it is SN type Ia or a core-collapse SN, but it might not apply to the rare types such as type Ib and Ic [36]. To estimate how the SN energy budget contributes to the CR energy density, we need to know the fraction η_{CR} of energy transferred from SN into powering CRs; the frequency r_{SN} that such events happen; the average time τ_{CR} that CRs reside in our Galaxy; and a confinement volume of the Galaxy V_{gal}. One can estimate the CR energy density in our Galaxy introduced by SNR with:

$$\epsilon_{CR} = \frac{\eta_{CR} E_{SN} r_{SN} \tau_{CR}}{V_{gal}}. \tag{2}$$

The mechanism proposed for a SNR to accelerate CRs is diffusive shock acceleration (DSA) [44], which we will discuss about in detail in Chapter 3. Several decades of studies of DSA at SNR have suggested an efficiency of above $\sim$ 10% of the SN kinetic energy release going into powering CRs [45]. The rate of SN events in our Galaxy is on average 3 per 100 years [46]. As we will mention in section 2.3, CRs at GeV energies reside in our Galaxy for $\sim$15 Myr calculated from the measured chemical abundance ratio of the secondary to primary elements from spallation [47]. Finally, we consider the galaxy as a disk of a 15 kpc radius and a 500 pc height. The volume of the galaxy is then $V_{gal} \simeq 350$ kpc^3. This leads to a CR energy density $\epsilon_{CR} \sim$2.5 eVcm^{-3}, which is consistent with the order of magnitude of 1 eVcm^{-3} measured in our Galaxy. Furthermore, DSA at SNR leads to a power-law spectrum of CRs. DSA predicts a power-law slope of 2, which is harder than the observed CR spectrum below the 'knee'. This effect is explained by the propagation of CRs in the Galaxy [48]. In addition, observations of SNR in radio emission, X-ray and gamma-ray are indications of non-thermal radiation from ultra-relativistic electrons and ions, and signatures of CR acceleration at SNR [36, 48–50]. The shell structure needed for DSA to take place in SNR is resolved spatially in a number of TeV gamma-ray observations [51–55], which added

more pieces of evidence that SNRs are responsible of accelerating GCRs.

However, both, observations and acceleration models can hardly allow for PeV acceleration at SNR. CRs accelerated by DSA in SNR were realized to have exceedingly low maximum energy [6]. Thereafter, extensions to the model were investigated, such as the streaming instability from the plasma responding to the moving CRs resulting in the amplification in magnetic fields [56]. This results in a more intense acceleration of CRs, but the maximum energy is still only up to $\sim$ 100 TeV, which is one order of magnitude below the 'knee' [7]. Therefore, other candidates of Galactic PeV-atrons are proposed to explain the high-energy GCRs, such as star clusters [8, 18].

2.2.2 *CRs from Star Clusters*

A star cluster is a collection of stars forming at approximately the same time as the result of a gravitational collapse of a giant molecular cloud [57]. Young and massive star clusters blow out strong collective stellar wind that sweeps out the nearby interstellar medium (ISM) and form bubbles. Star cluster wind bubbles have been resolved in observations in the optical range and X-ray of Westerlund 2 [58], and in infrared of Quintuplet [59, 60], and they are proposed as candidate sites to accelerate GCRs [11, 61–64]. A series of observations have confirmed gamma-ray emission from the vicinity of nearby star clusters in GeV (i.e. [15]) and TeV ranges (i.e. [65]), indicating non-thermal processes in these regions. As an example, Fig. 2 shows the excess map of observed gamma-rays from the region overlapping Westerlund 2 [66]. The extended spatial distribution of gamma-ray emission around the star cluster supports the surrounding wind bubble as a possible CR acceleration site. The gamma-ray observations are used to study the CR energy budget and spatial distribution. Yang et al. (2019) [11] showed that the efficiency of the star cluster wind kinetic energy converted to CRs through acceleration can be $\sim$ 10%, and PeV CR energy can be reached. As we will see in Chapter 4, a collective wind with a benchmark value of a kinetic wind luminosity of the order of 10^{38} erg s^{-1} is energetic enough to accelerate CRs to $\sim$ PeV.

2.3 PROPAGATION OF COSMIC RAYS

It was mentioned in Section 2.1 that CRs gyrate around magnetic field lines as they propagate. However, the magnetic fields in astrophysical environments are largely unknown and often with a high level of turbulence. As we will see in detail in Chapter 3, perturbations in magnetic fields lead to an important property of CR propagation called diffusion. The diffusion results in unpredictable and random paths when CRs travel from their sources to the Earth. The evidence is seen indirectly in our Galaxy in the chemical abundance of CRs.

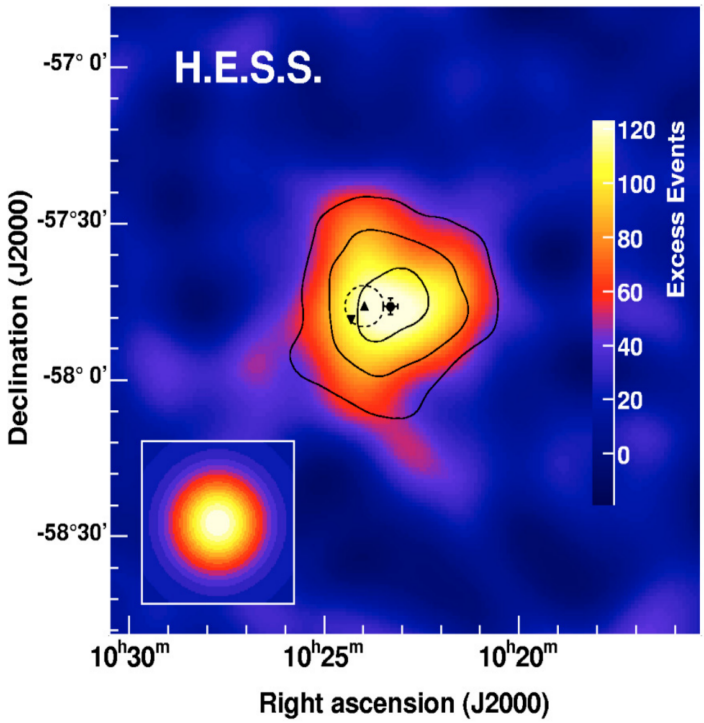

Figure 2: Correlated excess sky map with an oversampling radius of 0.12° of the Westerlund 2/RCW 49 region. (Figure by [66])

As shown in Fig. 3, overabundances in some light elements such as Lithium (Li), Beryllium (Be), and Boron (B) in GCRs have been measured compared with the chemical abundance of our solar system, which represents elements from the Big Bang nucleosynthesis, stellar nucleosynthesis and processes related to the death of stars [67]. The overabundances in these elements are caused by spallation when heavy CR nuclei (mainly Carbon (C), Nitrogen (N) and, Oxygen (O)) collide with ISM gas. The collision results in production of the lighter elements. By this mechanism, the abundances of Li, Be and B abundance increases by a factor of $\sim 10^4$ compared to that of the solar system [68]. The relative primary to secondary chemical abundance is used as a 'clock' to measure the time that CRs have resided in our Galaxy. Measurement by CRIS of low energy CRs ($\sim$70 to $\sim$400 MeV nucleon^{-1}) have yielded a $\sim$15 Myrs residence time of GCRs with GeV energies [47]. In contrast, the propagation time would only be $\sim$2000 yrs at 400 MeV assuming ballistic propagation of CRs. Therefore, the effect of CR diffusion is significant in CR propagation. Furthermore, because diffusion also happens in the source where they are accelerated, it is an essential property to take into consideration in understanding the acceleration of CRs. The diffusion impact on the acceleration process will be introduced in chapter 3.

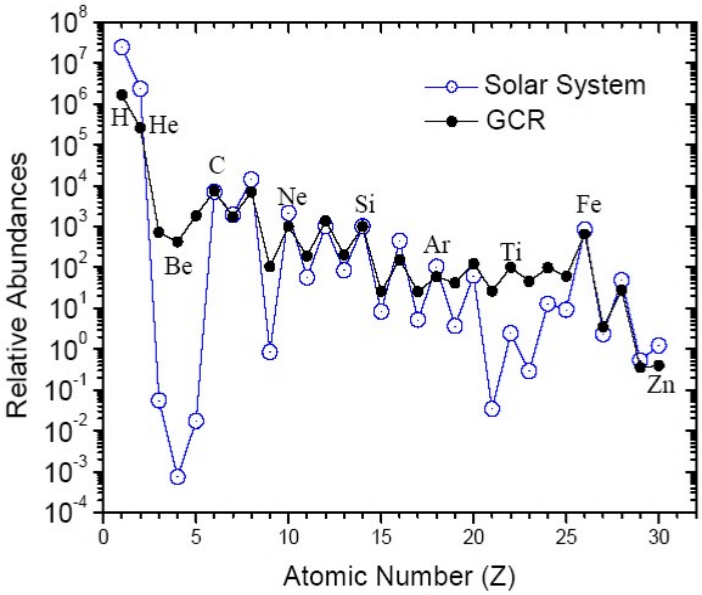

Figure 3: The measured CR chemical abundance compared with the present-day solar system material (Figure by [67])

2.4 MULTI-MESSENGER INVESTIGATION

Multi-messenger astrophysics emerged in the last few decades with the advancement of knowledge of non-photonic messengers and their detection technology. In addition to observations across the electromagnetic spectrum (i.e. radio, infrared, optical, UV, X-ray, and gamma-ray), also CRs, neutrinos, and gravitational waves have entered the picture. Utilizing different messenger properties and understanding the messenger relations extend the potential to probe high-energy phenomena and violent systems. In the case of CRs, their diffusive nature makes it challenging to trace them back to their sources. Thus, we aim to relate a high-energy CRs to other messengers. In this section we will talk about the processes relating the high-energy CR to the gamma-ray and neutrino in subsection 2.4.1; in subsection 2.4.2, we discuss some basic properties and aspects of the observation of CRs, gamma-rays, and neutrinos.

2.4.1 *Process of Secondary Gamma-ray and Neutrino Production*

The focus of this project is on the prediction of high-energy neutrinos and gamma-rays from our candidate Galactic PeV-atron: star clusters. With a population of relativistic high-energy CR protons in the system, we expect that interactions of these CRs with the ambient gas produce secondary particles such as neutrinos and gamma-rays. This effect was noticed during the 1970s in term of its significant role in gamma-ray and neutrino astronomy [69, 70]. The leading process is the inelastic collision of high-energy CRs with gas producing π^0 and $\pi^{\pm}$. Due to isospin symmetry of strong interactions, π^+, π^-, and π^0 are produced at

similar rates [71]. The decay of π^0 leads to gamma-ray production: A charged pion decays into a muon and a muon neutrino.

$$\pi^0 \rightarrow \gamma\gamma, \qquad \pi^+ \rightarrow \mu^+\nu_\mu, \qquad \pi^- \rightarrow \mu^-\bar{\nu}_\mu.$$

The muon further decays into a electron or positron, an electron neutrino, and a muon neutrino.

$$\mu^+ \rightarrow e^+\nu_e\bar{\nu}_\mu, \qquad \mu^- \rightarrow e^-\bar{\nu}_e\nu_\mu.$$

Therefore, we would expect gamma-rays, electrons or positrons, electron neutrinos/anti-neutrinos, and muon neutrinos/anti-neutrinos as the final products of the high-energy interactions of CRs. In a range of proton energy from GeV to TeV, around 17% of the proton kinetic energy $E_{p_{kin}} = E_p - m_p c^2$ transfers to each pion produced from the collision [72]. The average gamma-ray energy $\langle E_\gamma \rangle$ and neutrino energy $\langle E_\nu \rangle$ in relation to the primary proton energy are $\langle E_\gamma \rangle / E_p = 0.1$ and $\langle E_\nu \rangle / E_p = 0.05$ respectively [73].

Pion production and decay at the source produces electron neutrino, muon neutrino, and tau neutrinos are and are produced with a ratio of (1:2:0) [71]. During the propagation of neutrinos from the source to the observer, their flavors 'oscillate'. As a result, all three flavors of neutrino ν_μ, ν_e, and ν_τ are expected when the neutrinos are observed from a distance. For astrophysical sources, a flavor equipartition of neutrinos is expected at Earth.

2.4.2 *Observational aspects of CR, gamma-ray and neutrino*

The method of CR detection differ depending on the CR energy. The detection of sub-'knee' CRs (up to $\sim 10^{14}$ eV) are possible by direct detection with satellites and balloons. Direct CR observations provide us with information on the energy spectrum and chemical composition. Above 10^{15} eV, the flux of CRs arriving at Earth drops to a few tens of particles $\mathrm{m}^{-2}\mathrm{yr}^{-1}$. Detection of such low flux is no longer possible due to the small effective areas of the detectors, which is defined as the geometric area of the detector times the detection efficiency [71]. Instead, detection of these energies can be achieved by ground based detectors [74]. The ground based observatories detect the air shower initiated by primary CRs. A cascade of secondary particles are produced when the primary CRs interact with an atmospheric nucleon [72]. Short-lived secondary hadrons further decay into lighter nucleons, high-energy photons, electrons/positrons, muons/anti-muons, and neutrinos. These particle showers can be observed by extended ground arrays of detectors (water Cherenkov or scintillators) as well as by air fluorescence light emitted along the shower core. With this approach, the flux, mass, and directional information are studied up to the highest energy CRs [71]. Since the arrival directions of CRs do not point back to their sources, the origin of CRs need to be studied from complementary messengers: photon and neutrino.

The interactions of high-energy CRs result in the source shining in gamma-rays and neutrinos. For gamma-rays, other than their hadronic origin from π^0 decay, there are possibly also leptonic contributions to the total gamma-ray emission, such as inverse Compton emission, and bremsstrahlung from relativistic electrons. Thus, both leptonic and hadronic gamma-ray emission need to be considered when it comes to interpreting gamma-ray data. In general, gamma-ray observations are carried out, both in space and on ground. The Earth's atmosphere is opaque to gamma-rays. Therefore, detection in space became the primary approach. From keV to a few GeV gamma-ray is covered by various satellite telescopes [71, 75]. At higher energies, gamma-rays can be observed by ground-based experiments. high-energy gamma-rays interact with matter at the top of the atmosphere and produce a shower of particles. The Cherenkov radiation from these air shower is detected by so-called Imaging Atmospheric Cherenkov Telescopes (IACTs), which are very effective in studying higher than a few tens of GeV gamma-rays [76].

high-energy gamma-rays interact very easily with the cosmic background photons like the cosmic microwave background via pair production:

$$\gamma + \gamma \rightarrow e^+ + e^-. \tag{3}$$

Therefore, energetic gamma-rays are highly attenuated over large distances. For instance, PeV energy gamma-ray have an interaction length of about 10 kpc limiting observations of Galactic source [71]. Since the star clusters that we are interested in are Galactic sources, the study of them through gamma-ray observation is feasible, but the absorption by star light could play a non-negligible role.

Unlike gamma-rays, high-energy neutrinos are messengers unique to hadronic processes. Therefore, studying neutrino productions is a promising way of understanding the CR protons in the star cluster. Due to the weak interaction of neutrinos, they do not get influenced by the magnetic field and do not interact or get absorbed by dust and photons when traveling. Thus neutrinos trace directly back to the source without attenuation in the flux even from a large distance. It makes the neutrino an ideal messenger to study both Galactic and extra-galactic phenomena. However, the weak interaction brings significant difficulties in astronomical neutrino observations.

From interactions of CRs reaching PeV energies, we expect neutrinos with energies up to $\sim 10^2$ TeV. One major detection technique for high-energy neutrinos is based on the radiation of optical Cherenkov light produced by relativistic charged particles. For example, the charged current interaction of muon neutrinos with nucleons (N), via deep inelastic scattering:

$$\nu_\mu + N \rightarrow \mu^- + X. \tag{4}$$

This interaction is utilized by IceCube, currently the largest optical Cherenkov neutrino detector located at the South pole, which has the ability to detect neutrinos above 100 GeV [77]. Because of the low interaction rate of high-energy neutrinos, the detector has to be large enough to allow neutrino interactions. The IceCube detector monitors one cubic kilometer of clear Antarctic ice via an array of optical modules containing photomultiplyer tubes. When the interaction shown in (4) happens, the muon loses energy through bremsstrahlung, pair production, and photo-nuclear interactions in the ice [78]. As the muon passes through the detector, the muon and secondary particles from its interaction with matter leave traces of Cherenkov light, which allows to reconstruct the neutrino event with an angular resolution of typically $\leq 1^\circ$ [79]. Furthermore, IceCube also detects Cherenkov light of hadronic cascades resulting from neutral current events of any-flavor neutrinos and the charged current event of electron neutrinos. The reconstructed angular resolution of cascade events is around $10^\circ - 15^\circ$ [80].

3

TRANSPORT EQUATION AND DIFFUSIVE SHOCK ACCELERATION

To unravel the mystery of how CRs are accelerated up to PeV energies in the Galactic environment, it is important to realize the possible mechanism that accelerates charged particles efficiently. Diffusive shock acceleration (DSA) based on the theory of *first-order* Fermi acceleration was discovered in the 1970s by several independent works [81–84]. Its success in modeling galactic CR acceleration can be described for the following reasons: 1) It leads to an power-law distribution CR differential spectrum; 2) It is an efficient mechanism to accelerate charged particles; 3) The ingredients required for DSA to take place, shock and plasma, are ubiquitous in the Galaxy.

In this chapter, we approach DSA, both, qualitatively and quantitatively. The layout of this chapter is as follows. We dive into the quantitative discussion on CR diffusion in Section 3.1. Then, we introduce the mechanism of DSA in section 3.2 with a physical approach. Thereafter in Section 3.3, the transport equation is introduced as a quantitative approach to derive DSA. It is applied to a planar shock as an example. The impact of the boundary conditions of the shock on particle acceleration is discussed in subsections 3.3.1 and 3.3.2.

3.1 CR DIFFUSION

The diffusive motion of CRs is a result of the scattering by irregularities in magnetic fields [19]. In astrophysical environments, perturbations in the magnetic fields are often present, such as hydrodynamic waves moving at the Alfvén speed [85]. Therefore, diffusion plays an important role in CR transport and acceleration. CR diffusion is quantitatively described by the diffusion coefficient D, which parameterized how fast a property (e.g. pitch angle, momentum, and replacement in space) of CRs changes over time. One can derive the diffusion coefficient from the motion of a charged particle in a large-scale magnetic field B_0 with a perturbation δB. Detailed calculation can be found in e.g. Blandford & Eichler (1987) [44], and Blasi (2013) [36].

The diffusion coefficient in space has a dimension of L^2T^{-1}. It describes how fast CR

particles 'spread' over an area in space. The average diffusive area that a particle with a velocity v diffuses over a time t is:

$$\langle d^2 \rangle \sim \lambda(vt) = Dt\,, \qquad \lambda \equiv \frac{D}{v}, \tag{5}$$

where λ is defined as the diffusion length over which a particle travels before its pitch angle changes significantly. The diffusion length can also be expressed as $\lambda = v\tau$, where τ is the diffusion time.

CR diffusion is efficient when the Larmor radius is comparable with the length scale of the disturbance [86]. For CR resonant scattering in a three dimensional space with isotropic velocity v, the spatial diffusion coefficient is [36]:

$$D = \frac{1}{3}v(v\tau) \simeq \frac{1}{3}v^2\Omega^{-1}\left(\frac{k\mathcal{P}(k)}{B_0^2/8\pi}\right)^{-1} = \frac{1}{3}\frac{R_L v}{\mathcal{F}} \tag{6}$$

where $\mathcal{P}(k)$ is the power spectrum of the turbulence, which describes the wave energy density in the wave number range dk at the resonant wave number k. $\mathcal{F}$ is related to the power spectrum and is defined as: $\mathcal{F} = \left(\frac{k\mathcal{P}(k)}{B_0^2/8\pi}\right)$. The factor Ω equals to v/R_L, and B_0 is the background magnetic field. In this project, we will investigate particle acceleration under three different assumptions of the spectra of the turbulence in the plasma. They result in different dependencies of the diffusion coefficients $D(p)$ on the CR momentum p. $\mathcal{F}$ can be approcimated in terms of Larmor radius and the coherence length L_c of the perturbed system: $\mathcal{F} = (\frac{L_c}{R_L})^{1-\delta}$. The detailed derivation can be found in Appendix. The coherence length L_c is the largest scale at which the turbulence is injected. Therefore, the diffusion coefficient can be rewritten as:

$$D(p) = \frac{1}{3}cR_L(p)^{2-\delta}L_c^{\delta-1}, \tag{7}$$

where the value of δ depends on the assumption of the power spectrum of the turbulence. Here, we explore the cases of Bohm diffusion ($\delta = 1$), where the diffusion coefficient has a linear dependence on momentum; Kraichnan diffusion ($\delta = 3/2$) and Kolmogorov diffusion ($\delta = 5/3$) [87].

Bohm diffusion has the lowest value of diffusion coefficient at a given momentum. This is called the Bohm limit [42, 88]. When particles with a momentum which lead to $R_L(p) = L_c$ Bohm, Kraichnan and Kolmogorov diffusions become the same. For particles with larger Larmor radii than the coherence length of the system $R_L(p) > L_c$, the diffusion of particles changes regime to small angle diffusion. All diffusions start to follow: $D(p) \propto p^2$.

3.2 THE MECHANISM OF DSA

The essential ingredient for DSA is a shock wave. A shock wave is a propogation of disturbance in a medium faster than the sound speed. It is characterized by an abrupt change

in pressure, temperature, and density of the medium [19]. Shocks are common in several scales in the astronomical environment. The nearest case is the Earth's bow shock and the interplanetary shock [89, 90]. They are also found in SNR [86, 91], young stars [92], pulsars [93], planetary nebula [94], active galactic nuclei (AGN) [95], merging galaxy clusters [96], etc. The following is focused on the important properties of a shock and how charged particles can be accelerated at a shock.

Under the condition of an ideal gas, the sound speed in a medium is:

$$c_s = \sqrt{\frac{\partial P}{\partial \rho}} = \sqrt{\frac{\gamma k_B T}{\mu}}, \tag{8}$$

where P, ρ, and T are the pressure, density, and temperature of the gas respectively. k_B is the Boltzmann constant, γ is the adiabatic index, and μ is the mean molecular weight. When a shock propagates in a medium, the shocked fluid gets compressed and heated up. The sound speed in the shocked fluid increases and thus the fluid becomes subsonic. Discontinuities of the temperature, pressure, and density arises in the post-shock and the pre-shock material. In the rest frame of the shock front, a shock is described as an upstream medium moving towards the shock front and a downstream medium moving away from the shock. The upstream and downstream regions are separated by the discontinuity: the shock. A sketch of a planar shock is shown in Fig. 4. The strength of the shock is determined by the Mach number, where

$$\mathcal{M} = \frac{v_s}{c_s}, \tag{9}$$

where v_s is the velocity of the upstream fluid in the reference frame of the shock.

The connections in the upstream and downstream properties are studied by applying the equations describing an ideal fluid to a shock configuration, which includes the continuity equation, the equation of motion, and the conservation of energy. The result shows the upstream and the downstream properties depend only on the Mach number $\mathcal{M}$ and the fluid adiabatic index γ. For a shock with upstream properties u_1, ρ_1, P_1, T_1, and u_2, ρ_2, P_2, T_2 in the downstream, the condition of the discontinuity is described by the following:

$$\frac{u_1}{u_2} = \frac{(\gamma+1)\mathcal{M}^2}{(\gamma-1)\mathcal{M}^2+2} = \frac{\rho_2}{\rho_1}, \tag{10}$$

$$\frac{P_2}{P_1} = \frac{2\gamma\mathcal{M}^2-(\gamma-1)}{\gamma+1}, \tag{11}$$

$$\frac{T_2}{T_1} = \frac{(2\gamma\mathcal{M}^2-(\gamma-1))((\gamma-1)\mathcal{M}^2+2)}{(\gamma+1)^2\mathcal{M}^2}. \tag{12}$$

This set of relations is called the Rankine-Hugoniot jump conditions [97]. The shocked medium has a lower velocity, but higher pressure, density, and temperature compared to the pre-shock material. In the case of a strongest possible shock where $\mathcal{M} \to \infty$ of a

monoatomic gas ($\gamma = 5/3$), the compression in velocity is $u_1/u_2 = 4$. For a diatomic gas ($\gamma = 7/5$), $u_1/u_2 = 7$. It indicates that the higher the adiabatic index, the harder to compress the medium in a shock.

The original idea by Enrico Fermi on particle acceleration is based on the reflection of charged particles on a magnetized plasma moving at a velocity V in the galactic frame [98]. Each of such encounters leads the particle to gain or lose energy depending on their relative velocity. On average, a particle gains an energy fraction proportional to β^2 ($\beta = \frac{V}{c}$) during each encounter. This is therefore called *second-order* Fermi acceleration [98]. The original theory suggested interstellar clouds as the main sources of the 'magnetic mirrors'. However, since the random velocities of interstellar clouds are small, which are in the order of $\beta \leq 10^{-4}$, the acceleration mechanism is therefore relaticely inefficient [19].

The efficiency enhances significantly in a scenario when there are only head-on collisions. Particles only gain energy at the accelerator, and the average energy fraction gain per encounter is proportional to β. This is called the *first-order* Fermi mechanism, which is the theory adopted in DSA. DSA is characterized by a series of scatterings across a shock propagating in a medium [83]. The magnetic turbulence in the plasma causes the charged particles to diffuse on both sides of the shock. As a result, the average CR velocity on either side of the shock front is zero relative to the local flow. Therefore, the charged particles both in the rest frames of the upstream and downstream fluid perceive the fluid on the other side of the shock arriving against them. Particles with Larmor radii larger than the thickness of the shock can diffuse across the shock front. Each time when a particle travel from the upstream region to the downstream and returns, it gains a certain amount of energy.

We consider a particle that enters the shock from the upstream with an incident angle θ_{in} relative to the direction of the shock velocity U, and exits the downstream from an angle of θ_{out}. The upstream and downstream relative velocity is V, which for a strong shock is $V = (3/4)U$. Assuming the energy of the shock is unaffected by the 'collision' with a particle and the 'collision' is elastic, in the reference frame of the downstream, the particle's energy does not change as it enters and exits, which equals to:

$$E' = \gamma_V E(1 - \beta \cos\theta_{in/out}), \tag{13}$$

where, $\beta = V/c$, and γ_V is the Lorentz factor of the relative velocity. The primed quantities in this discussion are measured in the shock frame. Transforming from the downstream to the Galactic frame, the energy of the exited particle in the upstream becomes:

$$E_u = \gamma_V E'(1 + \beta \cos\theta'_{out}). \tag{14}$$

The change in energy of the particle from each cycle is:

$$\frac{\Delta E}{E} = \frac{E_u - E}{E} = \gamma_V^2(1 - \beta \cos\theta_{in})(1 + \beta \cos\theta'_{out}), \tag{15}$$

Because both the incident particles and the exiting particles are isotropic due to diffusive scattering. The following results holds from averaging the angles in between 0 and $\frac{\pi}{2}$:

$$\langle \cos\theta_{in} \rangle \simeq -\frac{2}{3} \qquad\qquad \langle \cos\theta'_{out} \rangle \simeq \frac{2}{3}. \tag{16}$$

The shock is assumed to be non-relativistic, thus $\gamma_V = 1$. With Eq. (15), the average energy gain the particles experience per cycle (from the upstream to downstream and back) is:

$$\left\langle \frac{\Delta E}{E} \right\rangle \simeq \frac{4}{3}\beta. \tag{17}$$

The energy fraction gain is linear to the relative upstream and downstream velocity V.

Note that the energy gain in Eq. (17) is counted per cycle. Particles with high enough energy escape the shock and do not get accelerated again. Before they escape, they experience multiple cycles of acceleration. After n cycles, a particle's energy change is $\Delta E \propto \beta^n$. We can reform this relation to connect the energy of an accelerated particle to its initial energy: $E = E_0\alpha^n$, where α is the fractional change in each cycle, and E_0 is the initial energy of the particle. From Eq. (17), it can be obtained that $\alpha = 4/3\beta + 1$. We then assume a probability P that a particle survives an acceleration cycle and remains in the acceleration site. For a starting population N_0 of charged particles, after n cycles of acceleration, we expect a remaining population $N = N_0 P^n$. Therefore, the distribution of the number of particles per energy can be derived:

$$N(E)dE \propto E^{-\gamma}dE, \tag{18}$$

where $\gamma = 1 - (\ln P / \ln\alpha)$. Based on the argument by Bell (1978), particles at the shock are injected at the rate of $\frac{1}{4}Nc$, where c is the speed of light [83, 99]. In the downstream, particles are advected away at the rate of $\frac{1}{4}NU$. This yields a surviving probability of $P = 1 - U/c$ [19, 83]. The power-law index γ can then be estimated:

$$\gamma = 1 - \frac{\ln P}{\ln\alpha} = 1 - \frac{\ln(1-U/c)}{\ln(1+U/c)} \simeq 1 - \frac{-U/c}{U/c} = 2 \tag{19}$$

Thus, a power-law distribution with an index of -2 is obtained from DSA.

3.3 TRANSPORT EQUATION AND DSA

The dynamics of CRs can be approached statistically using the Fokker-Planck formalism [70]. This leads us to a transport equation that we can apply to different astrophysical systems to investigate the CR transportation and acceleration as we will see in the following examples and Chapter 4. The distribution of CRs is described in terms of phase space density $f(z,p,t)$ (in 1D) in this formalism. It is related to the total number of CRs N_{CR} at a time t in the following way:

$$\int d^3z \int dp\, 4\pi p^2 f(z,p,t) = N_{CRs}(t), \tag{20}$$

where p is the CR momentum, and here we study the one dimensional transportation in the axis of z. The phase space density $f(z, p, t)$ describes information on how CR particles are distributed in space, time, and momentum space.

To describe CRs in a moving plasma, the transport equation is expressed in the Galactic frame. In 1D, it is written as (the detailed derivation can be found in Blandford & Eichler (1987) [44]):

$$\frac{\partial f}{\partial t} + u\frac{\partial f}{\partial z} = \frac{\partial}{\partial z}\left[D\frac{\partial f}{\partial z}\right] + \frac{1}{3}\left(\frac{\partial u}{\partial z}\right)p\frac{\partial f}{\partial p} + Q - L, \tag{21}$$

where u is the velocity of the plasma. The terms Q and L are the injection term and the loss term of CRs respectively. They act like a 'source' and a 'sink' of CRs in the system. Under the case of particle acceleration, term Q allows a mechanism that picks up a fraction from the thermal distribution of particles from the plasma and accelerates them to the non-thermal population. In the case of DSA, particles are only injected at the location of the shock front. The loss term L takes into account the scenario that there can be catastrophic energy losses leading to reduction in the CR population in the system. The first term on the left-hand-side of Eq. (21) is the time evolution term of CR phase space density; the second term is due to the advection of the plasma. On the right-hand-side, the first term is due to the diffusion of CRs; the second term describes the adiabatic energy loss of CRs in the moving plasma.

3.3.1 *Example 1: Infinite planar shock*

In the following, we will apply the transport equation (Eq.(21)) to a strong shock in order to quantitatively study DSA. Let us assume a planar shock as shown in Fig.4. The plasma in the upstream region has a constant velocity of u_1 and the downstream region has a constant velocity of u_2. We aim to obtain the phase space density $f(z, p)$ of accelerated particles. We assume the system to be stationary ($\frac{\partial f}{\partial t} = 0$), and the diffusion coefficient is spatially constant in the whole system.

We assume no catastrophic loss of CRs in the system. Therefore, the loss term $L = 0$. To have DSA, we need particles with Larmor radius larger than the thickness of the shock to penetrate through the shock front from the downstream region and get accelerated. These particles usually correspond to the ones with energies in the high-end of a thermal Maxwell distribution. The injection term $Q(z, p)$ allows such mechanism to take place at the shock. Let's introduce an injection fraction η_{in}, representing the fraction of the particle picked up from the thermal plasma at the shock front and accelerated. The injection of particles happens only to those with a momentum p_{in}, and only at the location of the shock front. Therefore, the injection term $Q(z, p)$ is in the following form:

$$Q(z, p) = \eta_{in}\frac{n_1 u_1}{4\pi p_{in}^2}\delta(p - p_{in})\delta(z) \tag{22}$$

where n_1 is the particle number density in the upstream region right before the shock, and u_1 is the upstream velocity. Let $f_1(z,p)$, $f_{sh}(p)$ and $f_2(z,p)$ be the phase space density in the upstream region, at the shock, and in the downstream respectively. Since $f(z,p)$ describes the accelerated particles which are injected at the shock front, it is expected be continuous across the shock. Therefore, we have the boundary condition:

$$f_1(0,p) = f_{sh}(p) = f_2(0,p). \tag{23}$$

We work under the assumption that the downstream region is homogenized due to the strong magnetic turbulence, namely $\partial f_2(z,p)/\partial z = 0$. The phase space density in the downstream $f_2(z,p)$ is spatially constant and is equal to $f_{sh}(p)$. Furthermore, there is no particle distribution and flux infinitely far in the upstream:

$$f(-\infty,p) = 0. \tag{24}$$

The solution can be found by integrating Eq. (21) first over the upstream region from $-\infty$ to 0; and over a infinitesimal region across the shock from $-\varepsilon$ to $+\varepsilon$ to obtain $f_{sh}(p)$. The solution to the CR upstream phase space density is:

$$f_1(z,p) = f_{sh}(p)\exp\left(\frac{u_1}{D(p)}z\right). \tag{25}$$

By intergrating across the shock front, we obtain:

$$f_{sh}(p) = S\left(\frac{p_{in}}{p}\right)^S \frac{\eta n_1}{4\pi p_{in}^3}, \tag{26}$$

where S depends on the compression ratio ($r = \frac{u_1}{u_2}$) at the shock: $S = \frac{3u_1}{u_2-u_1} = \frac{3r}{1-r}$. The phase space density at the shock front shows the acceleration of particles in the system. As shown in Eq. (26), $f_{sh}(p)$ is a power-law distribution with a slope of $-S$. The setup of a strong shock ($\mathcal{M} \gg 1$) yields $S = 4$, which means $f_{sh}(p) \propto p^{-4}$. With an estimate of the energy of relativistic particles $E = pc$, the following relation is derived:

$$\frac{dN}{dEdV} = f(E) \propto p^2 f_{sh}(p) \propto E^{-2}. \tag{27}$$

Where, $f(E)dE = 4\pi p^2 f(p)dp$. The solution of an infinite planar shock leads to a power-law spectrum of accelerated particles in agreement with the spectrum we derived from the previous section. However, there are some impractical aspects of this model. From the power-law of the phase space density $f_{sh}(p) \propto p^{-4}$, the following relation of the CR energy density ϵ with CR momentum is obtained:

$$\epsilon \propto \int dp\, p^3 f_{sh}(p) \propto ln\, p. \tag{28}$$

Since there is no maximum energy, the energy density diverges logarithmically with CR momentum under the setting of a strong shock. Furthermore, in an infinite sized shock, the

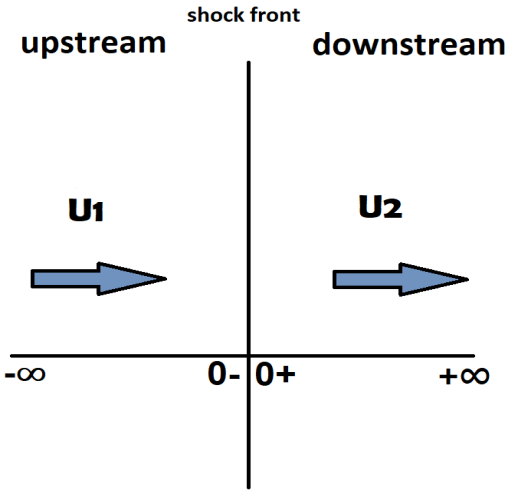

Figure 4: Illustration of an infinite planer shock: the shock front is located at z=0. u_1 and u_2 are upstream and downstream velocity respectively.

particles got injected into the system can not have a large enough Larmor radius to escape. With the continuous injection without any way to escape, an infinite amount of particles are trapped in the shock eventually. The trapped particles in a infinitely large system that lasts forever will keep getting accelerated to infinitely high energy. The stationary assumption therefore does not hold. To improve the model, we set a free escape boundary at radius z^* in the upstream region to allow accelerated particles to escape. The procedure and result will be presented in the next subsection.

3.3.2 *Example 2: Planar shock with a Free Escape Boundary*

Let us consider a system where the downstream region is the inside of the shock so that particles are only allowed to escape from the upstream region. In this case, we allow a free escape boundary at $z = z^*$ in the upstream. At the free escape boundary:

$$f(z^*) = 0, \tag{29}$$

there is no particle present. Beyond the point z^*, CRs are free to escape the system and would not return to the shock front to be accelerated again. We keep the assumptions that the system is stationary ($\frac{\partial f}{\partial t} = 0$) and CRs in the downstream region are homogenised throughout the space ($\frac{\partial f_2}{\partial z} = 0$).

We now apply again the transport equation (Eq. (21)) to the finite shock setup. Solve

the equation in upstream, and across the shock. The phase space density of accelerated particles in a finite shock is:

$$f_1(z,p) = f_{sh}(p)\frac{\exp\left(\frac{u_1}{D(p)}z\right) - \exp\left(\frac{u_1}{D(p)}z^*\right)}{1 - \exp\left(\frac{u_1}{D(p)}z^*\right)}. \tag{30}$$

The solution at the shock front becomes:

$$f_{sh}(p) = \frac{n_1\eta}{4\pi p_{in}^3} S \left(\frac{p_{in}}{p}\right)^S \exp\left(-S\int_{p_{in}}^{p}\frac{1}{p}\frac{1}{\exp\left(-\frac{u_1}{D(p)}z^*\right)-1}dp\right), \tag{31}$$

where S has the same definition as before ($S = \frac{3u_1}{u_2-u_1}$). Comparing to the solution for the finite shock (Eq. (31)) with that for the infinite shock setup (Eq. (26)), the presence of a free escape boundary introduced an exponential term to the power-law distribution. This leads to a maximum energy that particles get accelerated to at the shock. Once a particle gains a large enough energy, it has a high probability to escape the system from the upstream and would not travel back again to get accelerated. The diffusion length $\lambda = D(p)/u_1$ at the maximum momentum p_{max} is within the same order of magnitude as the escape length which in this case is $|z^*|$. As shown in the shock solution Eq. (31), the exponential cut-off is regulated by the ratio of the escaping length and the diffusion length.

Figure 5 shows the phase space density of accelerated particles at the shock front (z=0) under Bohm, Kraichnan and Kolmogorov. The result is obtained for the parameters stated in Table 1. The phase space densities under the three types of diffusion follow a power-law distribution of a slope of -2 at low energies and get suppressed after a certain energy. When $f_{sh}(p)$ drops one e-fold, we define the corresponding momentum as the maximum momentum p_{max} (which corresponds to the maximum energy E_{max} of particles from the acceleration). The phase space density of accelerated particle of energy E at the shock follows approximately $e^{-E/E_{max}}$. Comparing all three cases of diffusion, the accelerator is the most efficient at accelerating particles under Bohm diffusion. The Bohm diffusion coefficient has the lowest value and increases the fastest as momentum increases. Particles get accelerated to the highest energy and its phase space density gets suppressed the strongest at the cut-off energy. In the case of Kolmogorov, the diffusion coefficient has the highest value and grows at a slower rate as momentum increases. As a result, the particles gets accelerated to the lowest maximum energy with the mildest cut-off from the power-law distribution around E_{max}.

Figure 6 shows the spatial distribution of accelerated particles in the upstream region. The phase space density of particles with low momentum ($p \ll p_{max}$) and high momentum

u_1	10^8cm/s
p_{in}	1GeV/c
z*	1pc
L_c	1pc
B	100μG

Table 1: Benchmark parameters used to plot the solution of accelerated particle phase space density in a finite planar shock shown in Fig. 5 and Fig. 6

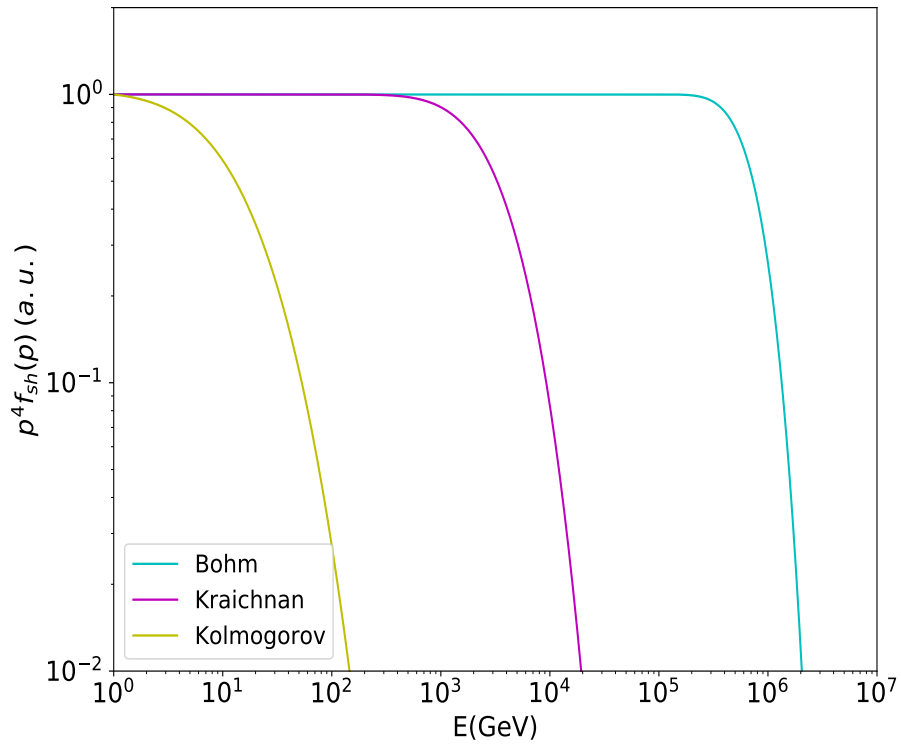

Figure 5: Spectra of CRs at the wind termination shock under scenario A. Three types of diffusion are compared: Bohm (blue), Kraichnan (margenta), and Kolmmogorov (yellow). The acceleration at the wind termination shock is the most efficient under Bohm diffusion.

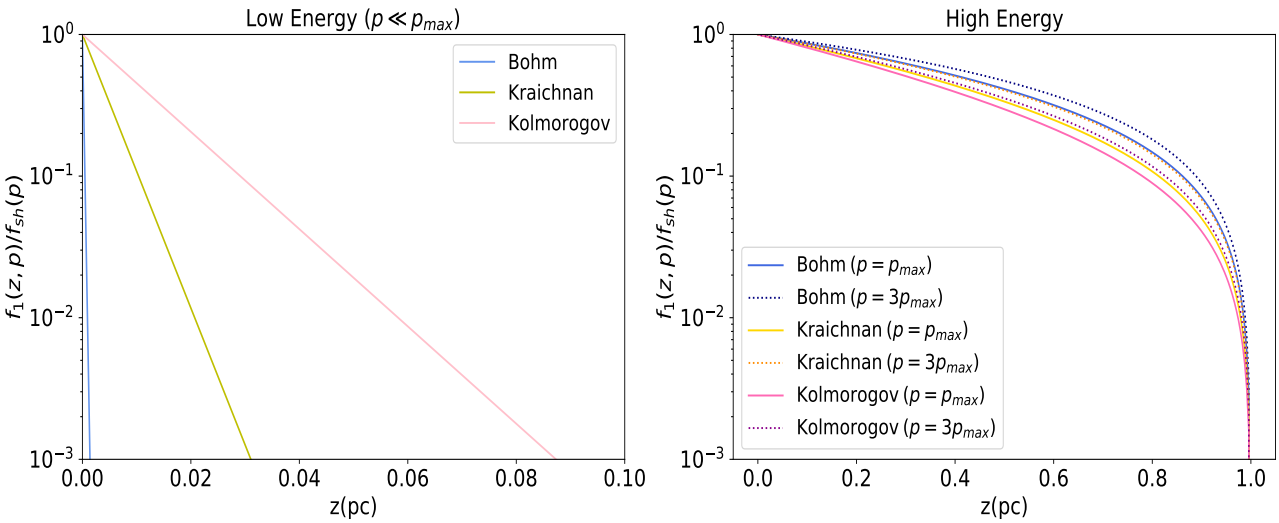

Figure 6: Finite shock phase space density in the upstream region normalized to which at the shock at different momentum. The horizontal axis shows the distance from the shock front in the upstream region. The shock is located at 0 and the escape boundary is z^* is at 1 pc. Low energy particles (left panel) and high energy particles (right panel) are compared. Low energy particles are mostly confined around the shock, while high energy particles diffuse further against the wind.

($p = p_{max}$ and $p = 3p_{max}$) under the three cases of diffusion are compared. The vertical axis shows the phase space density normalized to that at the shock, and the horizontal axis is the distance from the shock front in the upstream region. As shown in the plot on the left, the distribution of low energy particles vanishes very quickly around the shock location. On the other hand for high energy particles shown in the plot on the right, particles diffuse further against the upstream velocity and get suppressed at 1pc due to escape. It indicates that the low energy particles get mostly confined around the shock, while the high energy particles can diffuse far enough that the possibility that they diffuse back to the shock front and get further accelerated is negligible. The diffusion length for particles at E_{max} is comparable to the size of the system. The larger the diffusion coefficient, the longer the diffusion length thus the further a particle travels in the upstream region.

4

COSMIC RAY ACCELERATION AT STAR CLUSTERS

In this chapter, we specialize the DSA process in the context of the wind bubble inflated by a star cluster. We do so by solving the transport equation in 3D in a similar way as presented in the previous chapter for the case of the infinite planar shock. We eventually obtain not only the spectrum of accelerated particles, but also the spatial dependence of the phase space density of the accelerated particles at the source. This chapter is organized as follows: in Section 4.1, we describe the evolution and the structure of the star cluster inflated wind bubble; Section 4.2 introduces the profiles of the wind bubble linked to particle acceleration; Section 4.3 and Section 4.4 are devoted to the solution of the transport equation applied to two assumptions of the model of the wind bubble and the techniques used in solving the problem; the final Section 4.5 discusses the semi-analytical solution of the acceleration of particles and their spatial distribution. For some benchmark values of properties of the wind bubble, we compare the efficiency of acceleration at the shock under Bohm, Kraichnan, and Kolmogorov diffusion. The spatial distribution of high and low energy CRs inside the wind bubble are also investigated.

4.1 STAR CLUSTER BUBBLE STRUCTURE

Massive young star clusters are those systems hosting a large number of young stars such as OB and Wolf-Rayet stars localized in a compact parsec-sized region. Such cluster is typically younger than $\sim$ 10 Myr and has a total stellar mass of $\sim 10^4$ $M_\odot$ [100]. The intense activities of these young massive stars result in a strong stellar wind which at a sufficient large distance becomes collective and approximately spherically symmetric [61]. The wind blows material into the surrounding interstellar medium steadily and creates a cavity in the medium, which is called a star cluster wind bubble. The wind bubble goes under several stages in its evolution until the wind bubble becomes a pressure confined bubble when the internal pressure is comparable with that of the external ISM.

At an early stage of the evolution, since the swept-up interstellar medium mass is not comparable to the wind mass, the wind bubble is in a free expansion stage. Due to the high Mach number of the plasma, two shocks form as the bubble expands. A forward shock forms at the contact surface of the out-blowing wind and the ambient interstellar medium. It shocks

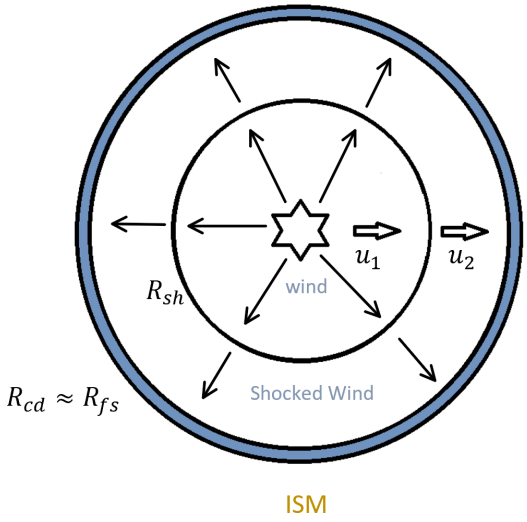

Figure 7: Star cluster wind bubble structure: The central region is the star cluster. R_{sh}, R_{cd}, and R_{fs} are the radii of where wind termination shock, contact discontinuity and the forward shock are located respectively. u_1 and u_2 are the upstream and downstream wind velocity.

the interstellar medium as it travels outward. A reverse shock forms which travels back into the wind in the wind reference frame. It is therefore called the wind termination shock forming within the out-blowing wind. The shocked interstellar medium and the shocked wind are separated by a contact discontinuity. So the wind bubble has evolved into a layered structure as shown in Fig. 7.

The shocked wind and the shocked ISM regions are initially radiative via thermal bremsstrahlung and turns non-radiative before the swept-up mass dominates the wind mass. When the wind bubble is non-radiative, it expands and cools adiabatically. The different cooling times of the shocked ISM and the shocked wind material result in the different expansion rates of the locations of the wind termination shock R_{sh}, and the forward shock R_{fs}. The cooling time is $t \sim 10^4$ yr for the shocked ISM, and is $t \sim 10^7$ yr for the shocked wind. The cooling time of the shocked wind is comparable to the age of such a wind bubble [101, 102]. Therefore, for most of the lifetime of a wind bubble, it stays in a configuration with a radiative shocked ISM at the outer layer, and an adiabatic wind region. Since the shocked ISM becomes cool and radiative, while the wind region keeps expanding adiabatically, the shocked ISM eventually gets compressed to a thin shell. Therefore, one can assume that approximately the locations of the contact discontinuity and the forward shock are the same $R_{cd} \approx R_{fs}$.

The star cluster that creates such a wind bubble is compact and contains up to ∼100-1000 stars in a radius of a few parsecs. The radius of the star cluster R_c is negligible compared to the location of the wind termination shock ($R_{sh} \gg R_c$). [103, 104]. McKee and Koo (1992) [101] introduced a model describing the evolution of the locations of the wind termination

shock and the forward shock as a function of the age of the wind bubble and the wind luminosity:

$$R_{sh} = 23(\frac{L_{w38}^3}{n_0^3 v_{in8}^5})^{1/10} t_6^{2/5} \quad \text{pc}, \tag{32}$$

$$R_{esc} = 66(\frac{L_{w38}}{n_0})^{1/5} t_6^{3/5} \quad \text{pc}. \tag{33}$$

Here t_6 is the age of the system in the unit of 10^6 yrs; n_0 is the hydrogen nuclei number density the unit of cm^{-3}; v_{in8} is the wind velocity in the unit of 10^8 cm s^{-1}; and L_{w38} is the wind Luminosity in units of 10^{38} erg s^{-1}. The wind luminosity is determined by the wind velocity and mass loss rate, which is the rate of mass injected by the wind into the bubble:

$$L_w = \frac{1}{2}\dot{M}u_1^2. \tag{34}$$

Assuming the age of the system to be 1 Myrs, a number density of hydrogen nuclei of $n_0 = 10$ cm^{-3} in the surrounding interstellar medium, with a wind velocity of u_1 =3000 km s^{-1} and a mass loss rate of $\dot{M} = 10^{-4}\, M_\odot$ yr^{-1}, the location of the wind termination shock according to the model is at $R_{sh} \approx 9$ pc and the escape boundary is at $R_{esc} \approx 51$ pc. This estimation shows that the wind bubble is dominated by the shock wind region. To further study the DSA of CRs in the wind bubble, properties such as the magnetic field and the shock condition need to be explored.

4.2 STAR CLUSTER PROFILES

Both of the expanding velocities of the wind termination shock and the forward shock are slow compared to the wind velocity. The forward shock moves outwards in a velocity of few tens of km s^{-1}[18], while the wind velocity is few 10^3 km s^{-1}. Since the timescales regulating the acceleration and transportation of CRs are small compared to the dynamical time of the system, the particle acceleration can be treated as stationary. The time dependent part of the transport equation (Eq. (21)) is therefore neglected. We assume that the bubble structure of the star cluster is spherically symmetric, depending only on radius r. The transport equation can be written in the form:

$$r^2 u_r \frac{\partial f}{\partial r} = \frac{\partial}{\partial r}[r^2 D \frac{\partial f}{\partial r}] + \frac{1}{3} p \frac{\partial f}{\partial p} \frac{\partial}{\partial r} r^2 u_r + r^2 Q. \tag{35}$$

The injection term Q is similar to the previous chapter:

$$Q(r,p) = \frac{\eta_{in} n_1 u_1}{4\pi p_{in}^2} \delta(p - p_{in}) \delta(r - R_{sh}), \tag{36}$$

where, we only allow injection of particles of a momentum p_{in} at the wind termination shock location R_{sh}. The injection efficiency η_{in} corresponds to the fraction of the incoming particle flux $u_1 n_1$ taking part in the acceleration. Therefore, CRs are injected at a total rate of:

$$\frac{dN_{CR}}{dt} = 4\pi R_{sh}^2 (\eta_{in} u_1 n_1) \tag{37}$$

The problem is effectively one dimensional. The center of the wind bubble (r=0) is the location of the star cluster, for which we ignore the size and treat it as point-like. Particles are picked up by the wind termination shock from the wind region and are accelerated at R_{sh}. Between the star cluster and the wind termination shock R_{sh} is the upstream of the shock. From the wind termination shock surface to the contact discontinuity where the shocked wind contacts with the shocked ISM is the downstream region of the shock. Because of the thin layer of the cold shocked ISM, we treat $R_{fs} \approx R_{cd}$. In the following calculation, we will consider two different scenarios of boundary conditions at the forward shock:

A) We assume a free escape boundary of particles at R_{fs}. Thus we have $R_{fs} \approx R_{esc} \approx R_{cd}$ (see Fig. 7). At R_{esc}, CRs are free to escape the system. We will thus obtain a solution of the CR phase space density in the upstream and the downstream regions of the wind bubble, and at R_{esc}, the phase space density is set to 0 due to the free escape boundary.

B) We investigate a more physical setup by considering the swept up ISM in between the contact discontinuity R_{cd} and the forward shock R_{fs}; and the ambient ISM surrounding the wind bubble. With this improvement to the model, the CR phase space density and flux are continuous at R_{fs}. The solution will include not just the upstream and downstream regions in the interior of the wind bubble, but also the dense cloud surrounding the wind bubble.

The wind termination shock is a strong shock with a large Mach number ($\mathcal{M} \gg 1$). The upstream properties and the downstream properties are connected via the Rankine-Hugoniot jump conditions. The velocity profile of the wind is:

$$u(r) = \begin{cases} u_1 = v_w & 0 < r < R_{sh}, \\ u_2(r) = \frac{u_1}{4}(\frac{R_s}{r})^2 & R_{sh} < r < R_{esc}. \end{cases} \tag{38}$$

The wind velocity $u_1 = v_w$ is approximately constant in the upstream region. While in the downstream region, the shocked wind is adiabatic and its velocity decreases proportional to its radial distance squared. Right across the wind termination shock R_{sh}, the property of the jump condition on velocity in a strong shock is preserved: $u_2(R_{sh}) = \frac{1}{4}u_1$.

Another important wind property is its mass loss rate $\dot{M}$. The mass density of the wind $\rho_1(r)$ depends on the mass loss rate $\dot{M}$ and wind velocity in the upstream region. The downstream mass density is then related to the upstream density at the shock via the jump condition. The downstream region is adiabatic and subsonic, thus the mass density is constant. The

following expression shows the density of the wind region and the shocked wind region respectively:

$$\rho(r) = \begin{cases} \rho(r)_1 = \frac{\dot{M}}{4\pi r^2 u(r)} & 0 < r < R_{sh}, \\ \rho(r)_2 = 4\rho_1(R_{sh}) & R_{sh} < r < R_{esc}. \end{cases} \tag{39}$$

In the upstream region, we assume that magnetic turbulence is generated with field strength determined by the condition that part of the wind kinetic energy into energy stored in the magnetic field. The magnetic field strength affects the diffusion coefficient of particles, which in turn regulates the acceleration and transport of high energy particles in the system. The parameter η_B gives the efficiency of the energy transfer from mechanical energy to energy stored in the magnetic field. The upstream magnetic field strength B follows the relation:

$$\frac{B^2}{8\pi} = \eta_B \frac{1}{2}\rho u^2. \tag{40}$$

Here, the left-hand-side is the mechanical energy times the efficiency coefficient of energy transfer, and the right-hand- side is the energy stored in the magnetic field. Using Eq. (39), the magnetic turbulence in terms of radius in the upstream is:

$$B_1(r) = \frac{1}{r}(\eta_B \dot{M} u_1)^{1/2}. \tag{41}$$

In the downstream region, the magnetic field is compressed in two dimensions by the shock surface, so that the compression factor in the downstream is $\sqrt{11}$ and stays constant in the downstream region [18]. Let B_2 be the magnetic field in the downstream. The relation is:

$$B_2 = \sqrt{11} B_1(R_{sh}). \tag{42}$$

The compression in magnetic field introduces differences in the upstream and downstream diffusion coefficient. By applying Eq. (42) to Eq. (7), the diffusion coefficient in the upstream and downstream can be written as:

$$D(r,p) = \begin{cases} D_1(r,p) = \frac{1}{3}\left(\frac{pc}{q_e B_1(r)}\right)^{2-\delta} c L_c^{\delta-1} & 0 < r < R_{sh}, \\ D_2(p) = \frac{1}{3}\left(\frac{pc}{q_e \sqrt{11} B_1(R_{sh})}\right)^{2-\delta} c L_c^{\delta-1} & R_{sh} < r < R_{esc}. \end{cases} \tag{43}$$

Here, L_c is the coherence length, which is the largest scale of turbulence. We assume that L_c is comparible to the size of the star cluster. The index δ varies depending on the assumption of the power spectra of the turbulence in the system. In the following calculation, Bohm, Kraichnan, and Kolmogorove are investigated, which correspond to δ =1, 3/2, 5/3 respectively. Because of the compression of magnetic field at the shock, the diffusion coefficient of particles is smaller in the downstream region than in the upstream region at the same particle momentum. For the case where we also consider the ISM outside of the wind

bubble, the CR diffusion in the ISM follows the Galactic diffusion coefficient. Therefore, the diffusion coefficient outside of the wind bubble is expressed as:

$$D_3(E) = 3 \times 10^{28} \left(\frac{E}{GeV}^{1/3} \right) \quad \frac{\mathrm{cm}^2}{\mathrm{s}}, \tag{44}$$

where E is the CR energy in GeV corresponding to the CR momentum p.

4.3 SOLUTION OF SCENARIO A

4.3.1 *Upstream Region*

The upstream region extends from the origin of the collective wind $r = 0$ to the wind termination shock at $r = R_{sh}$. Due to the spherical symmetry of the system, the net flux at the center $r = 0$ is zero, which means that the diffusion flux $D_1(0,p)\frac{\partial f_1}{\partial r}$ and the advection flux $u_1 f_1$ cancels out at $r = 0$. Due to continuity, at the wind termination shock R_{sh}, the upstream CR phase space density is normalized to which solved at the shock. Therefore the boundary conditions of the upstream region ($0 < r < R_{sh}$) are:

$$\left[D_1(r,p)\frac{df}{dr} - u_1 f_1(r,p) \right]_{r=0} = 0, \tag{45}$$

$$f(r = R_{sh}, p) = f_{sh}(p). \tag{46}$$

Now the transport equation in the upstream region reads:

$$r^2 u_1 \frac{\partial f_1(r,p)}{\partial r} = \frac{\partial}{\partial r}\left[r^2 D_1(r,p)\frac{\partial f_1(r,p)}{\partial r} \right] + \frac{1}{3} p \frac{\partial f_1(r,p)}{\partial p}\frac{\partial}{\partial r}(u_1 r^2). \tag{47}$$

Since injection of particles is only at the wind termination shock $r = R_{sh}$, the injection term $r^2 Q$ doesn't enter. Therefore there are only the advection term, diffusion term and adiabatic term describing the CR dynamics in the upstream. The upstream solution can be written in a compact way as:

$$f_1^A(r,p) = f_{sh}(p) \exp\left(- \int_r^{R_{sh}} \frac{V_{eff}(r,p;f_1)}{D_1(r,p)} dr' \right). \tag{48}$$

The effective velocity V_{eff} is introduced to simplify the form of the solution. It is defined as:

$$V_{eff}(r,p;f_1) = u_1 + \frac{G(r,p;f_1)}{r^2 f_1(r,p)}. \tag{49}$$

The term $G(r,p;f_1)$ is a function of the solution $f_1(r,p)$, which is defined as:

$$G(r,p;f_1) = \int_0^r \frac{\partial}{\partial r'}(r'^2 u_1)\frac{1}{3} f_1(r,p)\tilde{q}(r,p;f_1) dr. \tag{50}$$

Where, $\tilde{q}$ is also a function of $f_1(r,p)$:

$$\tilde{q} = -\frac{d\ln p^3 f_1(r,p)}{d\ln p}. \tag{51}$$

So that V_{eff} contains the information of the upstream wind velocity and adiabatic. Since $f_1(r,p)$ is included in the upstream solution, the solution is implicit.

As shown in Eq. (48), the upstream solution depends on the solution at the shock, which will be solved in section 4.3.3 from applying the transport equation to a infinitesimal region across the wind termination shock. The implicit solution will be converged with a recursive algorithm, and the final solution covering the whole wind bubble will be semi-analytical.

4.3.2 *Downstream Region*

The downstream region is the shocked wind region starting from the wind termination shock R_{sh} to the contact discontinuity approximately at R_{esc}. The shocked wind velocity in the downstream slows down proportional to radial distance squared:

$$u_2(r) = \frac{u_1}{4}\left(\frac{R_{sh}}{r}\right)^2$$

The adiabatic term in the transport equation vanishes because

$$\frac{\partial}{\partial r}\left(r^2\frac{u_1}{4}\frac{R_{sh}^2}{r^2}\right) = 0.$$

The injection term does not contribute in the downstream region because the injection is localized at the wind termination shock. Then the transport equation has only two terms left:

$$r^2 u_2(r)\frac{\partial f_2(r,p)}{\partial r} = \frac{\partial}{\partial r}\left[r^2 D_2(p)\frac{\partial f_2(r,p)}{\partial r}\right]. \tag{52}$$

The left-hand-side describes the advection due to wind, while the right-hand-side describes the diffusion of particles. Therefore the downstream solution is determined by the competition of diffusion against advection.

There are two boundary conditions in the downstream region ($R_{sh} < r < R_{esc}$). First, the solution of the downstream phase space density at the wind termination shock equals the solution at the shock, that we discuss in the next section. The second and third conditions are based on the assumption of a free escape boundary at the contact discontinuity. At the free escape boundary, the particle distribution is zero. Therefore, we have:

$$f_2(R_{sh},p) = f_{sh}(p), \tag{53}$$

$$f_2(R_{esc},p) = 0. \tag{54}$$

Furthermore, we define the CR flux at the escape boundary to be the escape flux:

$$-D_2(p)\frac{\partial f_2(R_{esc},p)}{\partial r} = j_{esc}(p). \tag{55}$$

After applying the boundary conditions, we arrive at the solution of the downstream region of scenario A:

$$f_2^A(r,p) = f_{sh}(p)\frac{1-e^{\beta(r,p)}}{1-e^{\beta(R_{sh},p)}}, \tag{56}$$

where, $\beta(r,p)$ has the expression of:

$$\beta(r,p) = \frac{R_{sh}^2 u_2(R_{sh})}{D_2(p)}\left(\frac{1}{R_{esc}}-\frac{1}{r}\right). \tag{57}$$

The downstream solution is analytical and is normalized to the phase space density at the shock. The exponents are regulated by the diffusion length of particles in the downstream D_2/u_2, the location of the forward shock R_{esc}, and the wind termination shock R_{sh}.

4.3.3 *Shock Surface*

Now, both the solutions for the upstream and downstream regions contain the solution at the shock $f_{sh}(p)$. To solve the phase space density at the shock, we consider a infinitesimal region across the shock in between $R_{sh}+\varepsilon$ and $R_{sh}-\varepsilon$, where $\varepsilon \to 0$. Since particles are injected and accelerated at the shock, the injection term Q is included in the transport equation. The transport equation now includes the advection term, the diffusion term, the adiabatic term and the injection term:

$$r^2 u(r)\frac{df}{dr} = \frac{\partial}{\partial r}\left[r^2 D(r,p)\frac{\partial f(r,p)}{\partial r}\right] + \frac{1}{3}p\frac{\partial f(r,p)}{\partial p}\frac{\partial}{\partial r}[r^2 u_r] + Q. \tag{58}$$

We integrate Eq. (58) from $R_{sh}-\varepsilon$ to $R_{sh}+\varepsilon$ to solve the equation. The solution at the shock f_{sh} in scenario A is obtained:

$$f_{sh}^A(p) = \left(\frac{p_{in}}{p}\right)^S S\frac{\eta_{in} n_1}{4\pi p_{in}^3} e^{-\Gamma_1} e^{-\Gamma_2}, \tag{59}$$

where Γ_1 and Γ_2 are regulated by upstream and downstream properties respectively:

$$\Gamma_1 = S\int_{p_{in}}^{p'}\frac{dp'}{p'}\frac{G(r,p;f_{sh})}{u_1 R_{sh}^2 f_{sh}}, \tag{60}$$

$$\Gamma_2 = S\int_{p_{in}}^{p}\frac{dp'}{p'}\frac{u_2(R_{sh})}{u_1}\frac{1}{1-e^{\beta(R_{sh},p)}}. \tag{61}$$

where, α has the same expression as in the previous section. S depends on the shock condition $S = \frac{3u_1}{u_1-u_2}$. $S = 4$ for a strong shock, which leads the solution to follow the p^{-4} power-law distribution. The exponential functions in Eq. (59) are regulated by upstream (Eq. (60)) and downstream properties (Eq. (61)) ,respectively. Since the solution is implicit in the upstream and at the shock, we introduce in the following the numerical method to find the solution.

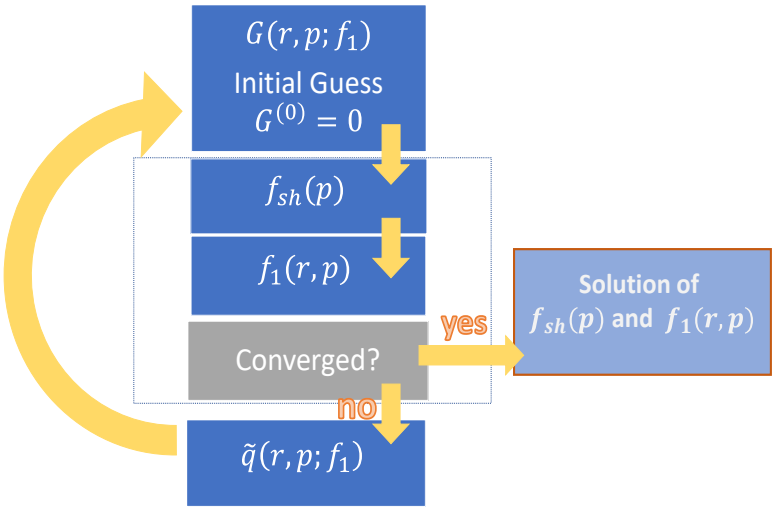

Figure 8: Iterative scheme taken to obtain the solution at the shock $f_{sh}(p)$ and $f_1(r,p)$. The iteration start with the guess function $G^{(0)}=0$. The solution is obtained once $f_{sh}(p)$ and $f_1(r,p)$ respectively converge.

4.3.4 *Iterative Solution*

The upstream solution depends both on itself, and the solution at the shock. While the solution at the wind termination shock contains itself. The co-dependence are embedded in $f_{sh}(p)$ (Eq. (59)), $f_1(r,p)$ (Eq. (48)); and the functions that are included in the expressions of these solutions: $G(r,p;f_1)$ (Eq. (50)) and $\tilde{q}(r,p;f_1)$ (Eq. (51)). We can solve this set of equation numerically via an iterative scheme shown in Fig. 8. We initiate the iteration with the guess function $G^{(0)}(r,p;f_1)=0$. With this choice, the 0th order solution at the shock $f_{sh}^{(0)}(p)$ can be analytically calculated. Then with $f_{sh}^{(0)}(p)$ and the guess function $G^{(0)}$, we can further calculate the 0th order upstream solution $f_1^{(0)}(r,p)$. Now we plug the 0th order $f_1^{(0)}(r,p)$ into Eq. (51) and then Eq. (50). The first order $\tilde{q}^{(1)}(r,p;f_1^{(0)})$ and $G^{(1)}(r,p;f_1^{(0)})$ can be obtained. With which the solution at the shock is updated with the 1st order $f_{sh}^{(1)}(p)$. The iteration continues in the order as shown in Fig. 8 until the solution is converged. An iteration scheme is developed in Python to perform this calculation.

To perform the calculation above, the constants that goes into the solution needs to be numerically determined, which include: the upstream wind velocity u_1, the wind mass loss rate $\dot{M}$, the conversion rate of the wind mechanical energy to the perturbation in the magnetic field in the upstream region η_B, the injection efficiency η_{in}, and the coherence length of

u_1	3×10^8cm/s
$\dot{M}$	$10^{-4} M_\odot$/yr
η_{in}	1.4×10^{-6}
η_B	0.1
L_c	1pc
T_{age}	1Myr

Table 2: Constants used in numerical calculation of the CR phase space density in star clusters

turbulence L_c. With these constants, the downstream wind velocity $u_2(r)$, the locations of the wind termination shock R_{sh} and the free escape boundary R_{esc}, and the diffusion coefficients $D_1(r,p)$ and $D_2(p)$ are calculated. The location of the wind termination shock R_{sh} and the free escape boundary R_{esc} are given by Eq. (32) and Eq. (33) according to the evolution of the wind bubble with its wind luminosity and the age of the star cluster. The benchmark values of the constants taken are summarized in Table 2, which are typical values for young massive star clusters.

The phase space density of cosmic rays in the wind bubble is studied under three cases of turbulence: Bohm, Kraichnan and Kolmogorov. The diffusion coefficients differs by their dependencies on the particle momentum. Figure 9 shows the individual iteration steps of the upstream solution at the shock location under Bohm diffusion. Note that at the shock, $f_1(R_{sh}, p) = f_{sh}(p)$. The iteration sharpenes the cut-off from the power-law distribution and lowered the E_{max}. As shown in the figure, the solution converges after 10 iterations. We check the converged solution numerically by inserting the solution of the upstream region $f_1(r,p)$ back in to the expression of the transport equation Eq. (47). The equation can be rearranged into the following form:

$$\left(r^2 u_1 - 2rD(r,p) - r^2 \frac{\partial D}{\partial r}\right) \frac{\partial f}{\partial r} = r^2 D(r,p) \frac{\partial^2 f}{\partial r^2} + \frac{2}{3} p \frac{\partial f}{\partial p} r u_1. \tag{62}$$

We calculated the two sides in Eq. (62) separately using the iterative solution, which are consistent with the identity.

4.4 SOLUTION OF SCENARIO B

In this section, the solution is calculated for the improved model where the ISM outside the wind bubble is also taken into consideration. We use the same method to solve the transport equation as in the previous scenario, but with different boundary conditions at the forward shock:

$$u_2(R_{fs}) f_2(R_{fs}, p) - D_2(p) \frac{df_2(R_{fs}, p)}{dr} = -D_3(p) \frac{df_3(R_{fs}, p)}{dr}, \tag{63}$$

$$f_2(R_{fs}, p) = f_3(R_{fs}, p). \tag{64}$$

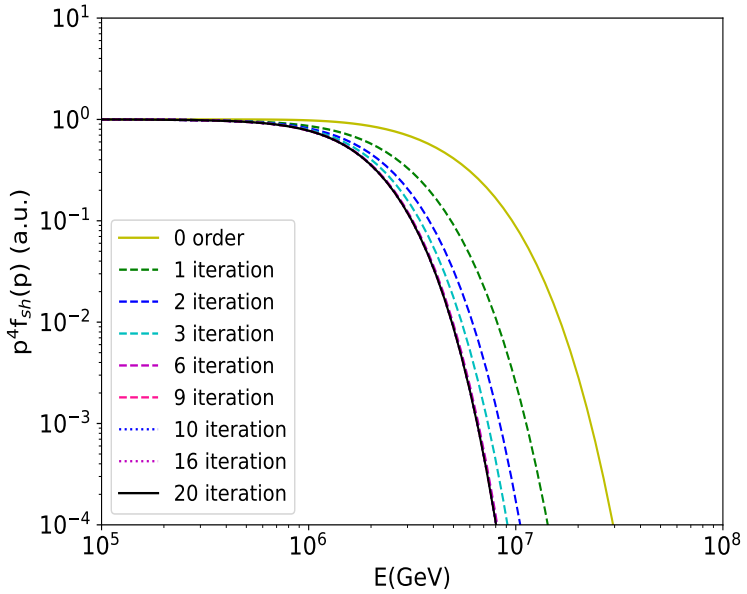

Figure 9: Iterations taken to obtain the converged solution at the shock $f_{sh}(p)$ under Bohm diffusion for scenario A: The yellow line shows the 0 order solution with the guess function G(r,p)=0. The black line is the solution after 20 iteration.

Here, f_3 is the CR phase space density in the region of the ISM. Eq. (64) means that the CR flux and phase space density is continuous at the forward shock. In the region outside of the wind bubble, we assume that the CR phase space density and flux vanish at an infinite distance:

$$f_3(\infty, p) = 0, \tag{65}$$

$$D_3(p)\frac{df_3(\infty, p)}{dr} = 0. \tag{66}$$

This model modifies the solution at the shock and in the downstream region due to the change of the boundary condition at the forward shock. The solution in the upstream region does not change its analytical expression compared to scenario A. The solution in the downstream region is now:

$$f_2^B(r, p) = f_{sh}e^{\beta(r,p)-\beta(R_{sh},p)}\frac{1+\alpha(p)(e^{-\beta(r,p)}-1)}{1+\alpha(p)(e^{-\beta(R_{sh},p)}-1)}. \tag{67}$$

Here, α has the form:

$$\alpha(p) = \frac{R_{fs}D_3(p)}{R_{sh}^2 u_2(R_{sh})}. \tag{68}$$

The function $\beta(r, p)$ in Eq. (67) is the same as that shown in Eq. (57), but with R_{esc} replaced by R_{fs} ($R_{esc} = R_{fs}$). The zone outside of the wind bubble has a CR phase space density of:

$$f_3^B(r, p) = f_{sh}\frac{R_{fs}}{r}\frac{e^{-\beta(R_{sh},p)}}{1+\alpha(e^{-\beta(R_{sh},p)}-1)}. \tag{69}$$

It has a spatial dependence of $f_3(r,p) \propto r^{-1}$. At a distance infinitely far away from the star cluster, $f_3(\infty,p) = 0$. The solution at the shock is:

$$f_{sh}^{B}(p) = \left(\frac{p_{in}}{p}\right)^{S} S\frac{\eta_{in} n_1}{4\pi p_{in}^3} e^{-\Gamma_1} e^{-\Gamma_3}, \tag{70}$$

Analogous to in the shock solution for scenario A (Eq. (59)), the exponents Γ_1 and Γ_3 are regulated by upstream and downstream properties respectively. The exponent Γ_1 is shown in Eq. (60), and Γ_3 is defined as:

$$\Gamma_3 = S\int_{p_{in}}^{p'} \frac{dp'}{p'} \frac{u_2(R_{sh})/u_1(1-1/\alpha)}{1/\alpha - 1 + e^{-\beta(R_{sh},p)}}. \tag{71}$$

The shock solution Eq. (70) compared to scenario A is slightly modified by Γ_3 due to the change in the downstream condition.

Similar to scenario A, the upstream solution and the shock solution are also implicit. Therefore, the solution can be derived numerically using the same iterative scheme introduced in Section 4.3.4 with the benchmark constants listed in table 2.

4.5 RESULTS

4.5.1 *Scenario A*

The full set of solutions describe the CR phase space density at any location inside the wind bubble. Fig. 10 shows the spectra of CRs at the radius of the wind termination shock. The phase space density of CRs is converted from momentum space to its corresponding energy space using the following relation:

$$f(r,E) = f(r,p) 4\pi p^2 \frac{\sqrt{m^2c^4 + p^2c^2}}{pc^2}. \tag{72}$$

The new quantity $f(r,E)$ has the unit of $GeV^{-1}cm^{-3}$. We investigate the acceleration of CRs at the shock under the three cases of turbulence: Bohm, Kraichnan, and Kolmogorov. CRs at the wind termination shock follow a power-law distribution up to around maximum energy E_{max}, after which the CR spectra steeply falls as energy increases. Among the three cases of turbulence, CRs get accelerated to highest energies under Bohm diffusion in comparison to Kraichnan and Kolmogorov diffusion. With a wind speed of 3000 km s^{-1} and a mass loss rate of $10^{-4} M_\odot/yr$, particles can be accelerated to PeV energies under Bohm diffusion. The maximum energy under Bohm diffusion is $E_{max} = 1.5$ PeV. Under Kraichnan diffusion, E_{max} is 40 TeV and is 570 GeV for Kolmogorove diffusion. The exponential suppression as the energy reaches E_{max} is the most rapid under Bohm diffusion and is the slowest under Kolmogorov diffusion.

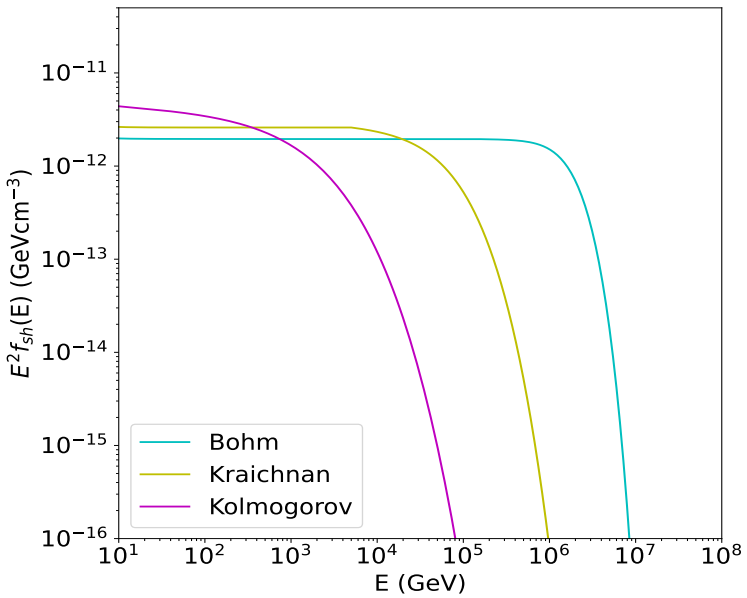

Figure 10: Cosmic ray spectra times E^2 at the wind termination shock under scenario A: the blue line features the CR spectrum under Bohm diffusion, the yellow line is the spectrum under Kraichnan diffusion and the magenta line is the spectra under Kolmogorov diffusion.

The different normalization of the spectra in Fig. 10 for Bohm, Kraichnan and Kolmogorov is due to the injection efficiency η_{in} in the normalization factor in the solution at the shock (see Eq. (59)): $p_{in}^S S \frac{\eta_{in} n_1}{4\pi p_{in}^3}$. The injection power η_{in} is calculated individually for different turbulence under an assumption of the test-particle-regime of CRs. It is assumed that at the shock location, the CR pressure reaches 5% of the wind ram pressure. Note that the percentage of the CR pressure to ram pressure can be varied under the range that CRs in the bubble do not play an active role in shaping the bubble properties. The assumption leads to the following relation:

$$\frac{1}{3}\int dp 4\pi p^2 p v(p) f_{sh}(p) \simeq 5\% \rho(R_{sh}) u_1^2. \tag{73}$$

To achieve the maximum injection efficiency under this limit, the efficiency η_{in} is tuned to satisfy the condition that the CR pressure is equal to 5% of the ram pressure at the shock. Due to the different solution of CR phase space density at the shock for Bohm, Kraichnan, and Kolmogorov, η_{in} is different as well.

Figure 11 shows the spatial distribution of CRs with high energies ($E = E_{max}$) and CRs with low energies ($E = 10\% E_{max}$) for Bohm, Kraichnan, and Kolmogorov. The vertical gray line denotes the locations of the wind termination shock (dotted) and the forward shock (solid). The region before this line is the upstream region. The region in between the vertical lines is the downstream region. In the upstream region, higher energy CRs can diffuse farther against the wind. The population of the low energy particles are suppressed drastically in the upstream region as going away from the shock against the wind. Most CRs get confined around the shock location.

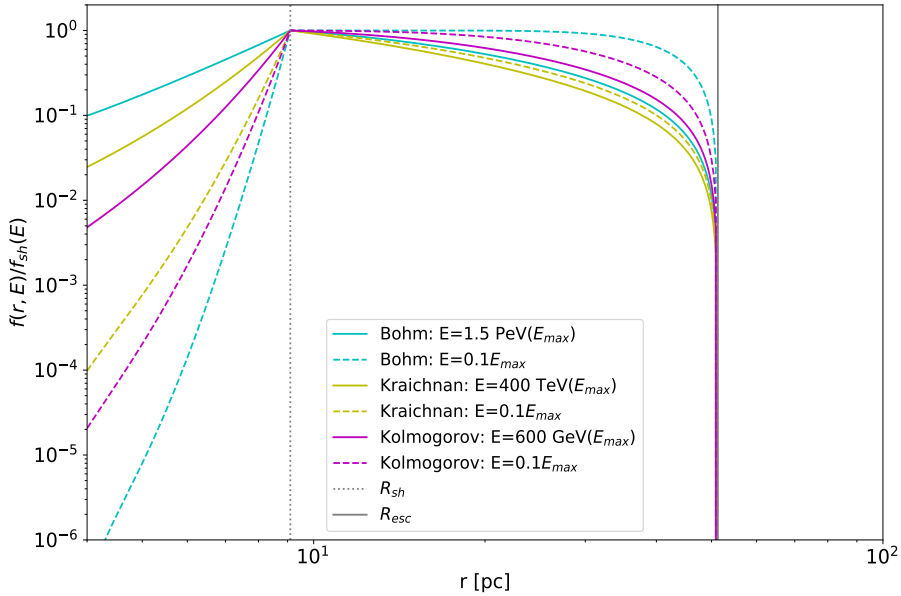

Figure 11: CR phase space density spatial distribution plotted at different energies under three types of diffusion for scenario A. The spatial distribution of high energy and low energy CRs are compared. The dotted gray line and the solid gray line are the locations of R_{sh} and R_{esc} respectively. The solid lines represents the high energy particles at E_{max}, and the dashed lines are CRs with 0.1 E_{max}

On the other hand, the downstream spatial distribution shows the effects of diffusion and advection on high and low energy particles. The low energy particles show a flat distribution, while the high energy particles are suppressed as the radius increases. Due to the larger effect of advection of the wind compared to the diffusion of low energy particles, they are more homogenized in the downstream. The diffusion and escape of high energy particles result in a more suppressed spatial distribution in the downstream region.

4.5.2 *Scenario B*

In scenario B, where we also include the ISM outside of the wind bubble, we only investigate CRs under Bohm diffusion, which is the most efficient case in accelerating particles as we have discussed in Section 4.5.1. Fig. 12 shows the spectrum of CRs at the wind termination shock. Compared to the spectrum based on scenario A, the modification in the shock solution is not significant. The shapes of the CR spectra under the two setups are almost identical, and the maximum energy of CRs stays around 1.5 PeV. Therefore, adding the region outside the wind bubble does not have a substantial effect on the acceleration of CRs at the wind termination shock.

The spatial distribution of CRs under Bohm diffusion in different regions is shown in Fig. 13.

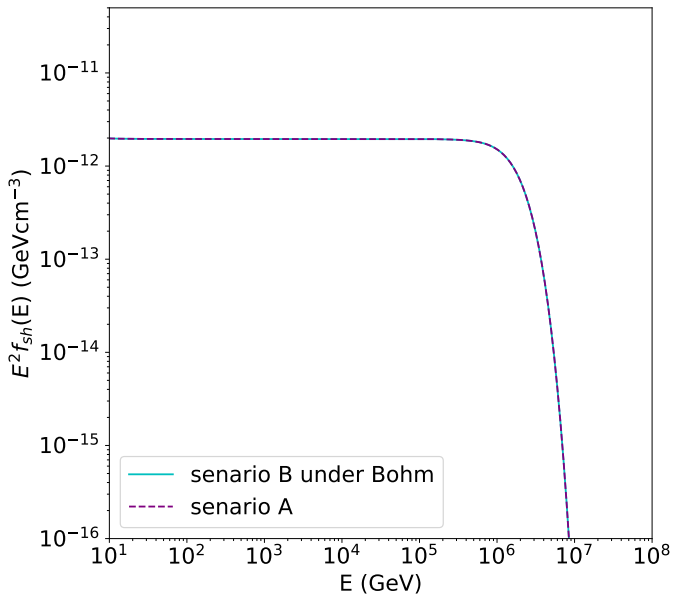

Figure 12: CR spectrum times E^2 at the shock under Bohm diffusion for the model including the outside ISM region. We compare the spectra obtained under scenerios A and B is for Bohm diffusion. No significant difference between the two solutions are visible.

The phase space density is normalized to that at the wind termination shock (vertical dotted line), and they are compared at 100 TeV, 1.5 PeV (E_{max}), and 2 E_{max}. The upstream region solution stays the same as in scenario A. The modification in the boundary condition at the forward shock now has a non-zero phase space density beyond R_{fs}. According to scenario A, the low energy particles have a more homogenized distribution in the downstream region because of the larger effect due to the advection of the wind compared to the diffusion of CRs. At the forward shock, the CR phase space density dropped 3-4 orders of magnitude compared to that at the shock and continuous into the ISM at $r > R_{fs}$. Regardless of CR energy, in the region outside of the wind bubble, the phase space density decreases with the distance from the star cluster as $f_3(r, p) \propto \frac{1}{r}$.

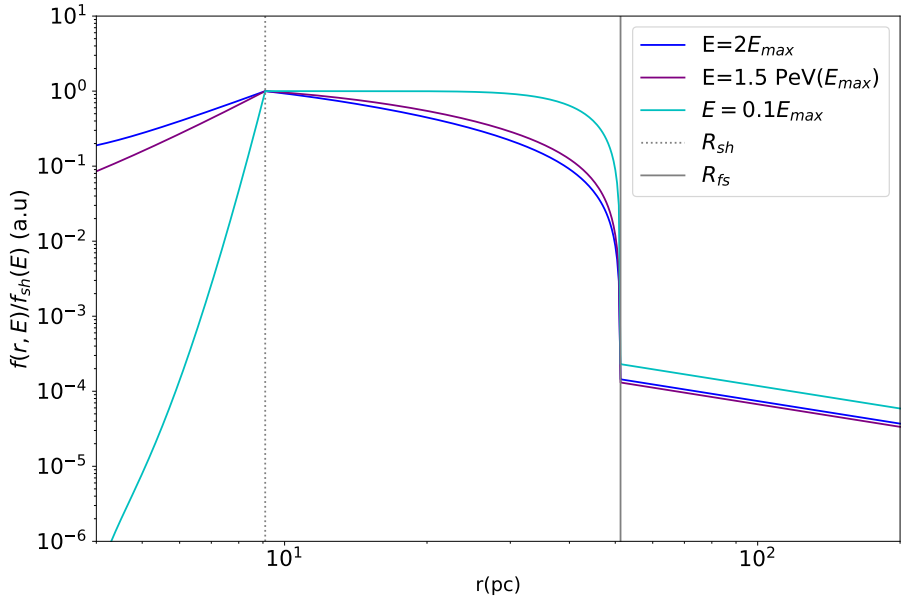

Figure 13: CR phase space density spatial distribution plotted at different energies under Bohm diffusion for scenario B. The spatial distribution of high energy and low energy CRs are compared. The dotted gray line and the solid gray line are the locations of R_{sh} and R_{esc} respectively. The purple and deep blue lines represents the high energy particles at E_{max} and $2E_{max}$, and the light blue line shows CRs with 0.1 E_{max}

5

MULTIMESSENGER INVESTIGATION

The CR phase space density calculated in a star cluster wind bubble supports that star clusters are plausible candidate Galactic PeV-atrons. The diffusive nature of CRs makes it challenging to probe the model via CR observations. Thus, we aim to relate the high-energy CRs in star clusters to the emissions from proton-proton (p-p) interactions when CR protons collide with the surrounding protons. In this chapter, we focus on the estimations of neutrino and gamma-ray productions at the source from CR interaction in the wind bubble in section 5.1, and the prediction of neutrino flux arriving on Earth in Section 5.2. The investigation of gamma-ray and neutrino emissions from specific sources and their observational aspects are discussed with the result.

5.1 PREDICTION OF NEUTRINO PRODUCTION AT SOURCE

In a star cluster wind bubble and its vicinity, neutrinos are produced through p-p interactions of CRs with the wind matter and the interstellar medium outside of the bubble. We calculate the neutrino and gamma-ray productions under the two scenarios discussed in Chapter 4: **A**) only the interior of the wind bubble is responsible for producing neutrinos; **B**) on top of the neutrino production from the wind bubble, the interactions of CRs with the surrounding shocked ISM and ambient ISM also contribute to the neutrino and gamma-ray emissions. The neutrino emission at the source of the two models will be compared and the contribution from different regions will be studied.

5.1.1 *The Target Material at Star Clusters*

The interaction rate of one CR proton with the surrounding matter is proportional to the target density n, the cross section of the p-p interaction σ_{pp}, and the CR proton velocity v ($v \approx c$ for relativistic particles):

$$rate = n(r)\sigma(p)v(p). \tag{74}$$

The target number density $n(r)$ is the only factor that has a radial dependence in Eq. (74). Assuming the target material is solely protons, the number density of target proton is related to the target mass density in the following way: $n(r) = \rho(r)/m_p$. The left panel of Fig. 14

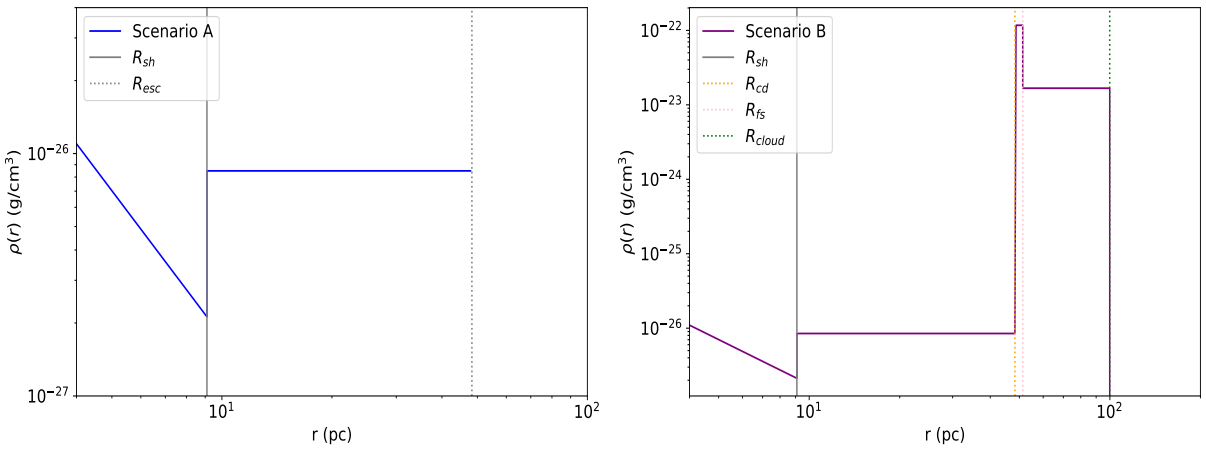

Figure 14: The target mass density under two scenarios are compared. Under scenario A (left panel), only the mass density in the upstream and downstream regions of the wind are considered. The gray solid line is the location of R_{sh}, and the dotted solid line is the location of R_{esc}. Under scenario B (right panel), three main regions of target material are taken into consideration: the wind region (upstream and downstream of the wind), the compressed ISM, and the ambient ISM. The location of the different regions are divided by the vertical lines at different radius. The upstream region is before R_{sh} (gray solid line); the downstream region is in between R_{sh} and R_{cd} (dotted orange line); the compressed ISM region is in between R_{cd} and R_{fs} (dotted pink line); and the ambient ISM is in between R_{fs} and R_{cloud} (dotted green line).

shows the target mass density inside the wind bubble which is applied to the calculation of the neutrino production under scenario A. The mass density $\rho(r)$ of the plasma in the upstream region depends on the wind mass loss rate $\dot{M}$ the wind speed u_1 (see Eq. (39)). Comparing to the target number density in the upstream region, the downstream target number density is larger by a factor of 4 at R_{sh} as a result of the compression at the wind termination shock.

The right panel of Fig. 14 shows the spatial dependence of the target mass density in different regions under scenario B. The upstream and the downstream wind region mass density are determined in the same way as in scenario A. The ISM surrounding the wind bubble has a denser number density of proton than the average ISM in the Galaxy. Here, we take the average number density $n_0 = 10$ cm^{-3} in the ambient ISM up to 100 pc from the star cluster [102]. It was discussed in Section 7 that the thin layer in between the contact discontinuity and the forward shock is the swept up ISM matter. The total swept up proton number is $N = (4/3)\pi R_{cd}^3 n_0$, and it is compressed in a volume of $(4/3)\pi(R_{fs}^3 - R_{cd}^3)$. It yields a target number density of around $7n_0$ by assuming $R_{cd} \approx 95\% R_{fs}$. Therefore, the target number density of the compressed ISM and the ambient ISM is 3-4 orders of magnitude larger than the wind.

5.1.2 *Estimation Methods*

In the following discussion, we introduce two methods to estimate the hadronic gamma-ray and neutrino emissions from p-p interaction. We begin with the approximation based on the average values of the lab-measured properties of p-p interaction. Then, we introduce a more precise calculation with the model introduced by Kelner et al. (2006) [105]. The model is based on simulations with the SIBYLL code of p-p interaction. In particular, we adopted the first method as an order of magnitude crosscheck for the complete calculation with the second method. The estimations with the two methods will be compared at the end of this section.

In the following approximation, we assume that in p-p interactions of CR proton with an energy E_P, neutrinos are produced with a fixed energy, corresponding to the average energy $E_\nu = \langle E_\nu \rangle$. On average, p-p interaction produces the same number of π^+, π^-, and π^0. From each charged pion, ν_e, ν_μ, and ν_τ are produced at the rate of (1:2:0) [71]. As mentioned in Section 2.4.1, on average, each leading pion produced from p-p interaction takes $\sim$ 20% of the CR kinetic energy. Subsequently, from pion decay and muon decay, each neutrino takes around 1/4 of the pion energy, which is equivalent to $\sim$ 5% of the initial CR energy. Here, we define the secondary to primary energy fraction in an interaction to be k, which is $k_\nu = \frac{\langle E_\nu \rangle}{E_p} = 0.05$ for neutrinos. The spectra of neutrinos is related to the CR spectra in the following way (the relation also holds for gamma-rays):

$$\frac{dN_\nu}{dE_\nu dV dt} = \frac{1}{k_\nu} M_\nu n \sigma_{pp} v f(r, E_p), \tag{75}$$

where $n(r)\sigma_{pp}v(p)$ is the interaction rate per CR particle that we already discussed. M_ν is the multiplicity, namely the number of neutrinos produced in each p-p interaction. A value of $M_\nu = 6$ is used for the estimation.

The cross section of p-p interaction $\sigma_{pp}(p)$ has a dependence on the proton energy [106]. After the threshold at a fraction of GeV, σ_{pp} grows quickly to $\sim 30 - 40$ mb (1 mb=10^{-27} cm^2) for few GeV. Afterwards, it grows logarithmically as energy increases. For the CR energy range from 10 GeV to 10 PeV, σ_{pp} can be assumed to be a constant of around 40 mb.

The same estimation method discussed above also applies for gamma-ray. From π^0 decay, there are two gamma-rays. Each gamma-rays takes $\sim$ 50% of the pion energy, which is $\sim$10% of the primary proton energy [71]. Therefore, for gamma-rays, the energy fraction $k_\gamma = \langle E_\gamma \rangle / E_p = 0.1$, and multiplicity M_γ=2. Comparing with the neutrino production, the spectrum of gamma-ray production follows the same trend but with the flux scaled and energy shifted:

$$\frac{dN_\gamma}{dE_\gamma} = \frac{M_\gamma}{M_\nu} \frac{k_\nu}{k_\gamma} \frac{dN_\nu}{dE_\nu}. \tag{76}$$

For an improved calculation of the secondary production from p-p interaction at the source,

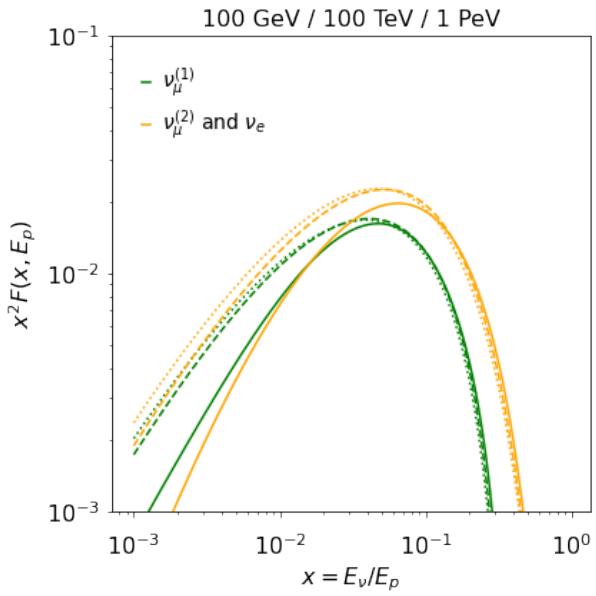

Figure 15: Neutrino spectra from pion decay and muon decay at proton energy E_p= 100 GeV (solid line), 100 Tev (dashed line), and 1 PeV (dotted line).

we adopted the model introduced by Kelner et al. (2006) [105]. It provides estimations of the production spectra of gamma-rays and neutrinos at each proton energy E_p. The total neutrino production spectra will be calculated by integrating over the proton energy range considering the CR spectra and the production rate. Since it provides the best accuracy on proton energy $E_p > 100$ GeV. The calculation is performed on the obtained CR spectra in Chapter 4 of the star cluster wind bubble above 100 GeV.

Since the calculation for gamma-rays and neutrinos follow similar forms, we focus on the neutrino production model in the following discussion. The model considers two types of neutrino production separately: muon neutrino from charged pion decay, and electron neutrino and muon neutrino from muon decay. An example of the scaled spectra from the model of neutrino production at different proton energies is shown in Fig. 15. It shows the neutrino spectra from pion decay and muon decay calculated at proton energies of 100 GeV, 100 TeV, and 1 PeV. In the first method of neutrino estimation introduced above, we assumed $k_\nu = 0.05$ regardless of the primary proton energy and neutrino flavor. As shown in Fig. 15 from this method, $k_\nu = 0.05$ is a reasonable assumption for the average neutrino energy as it corresponds to the location of the peaks of the distribution.

The production of ν_μ from pion decay, and ν_μ, ν_e from muon decay are computed separately and added together afterward. Each type of neutrinos production follows the relation below:

$$\frac{dN_\nu}{dE_\nu dV dt} = \int dE_p F(x, E_p) f_{CR}(r, E) \sigma_{pp}(p) n(r) v(p)). \tag{77}$$

Here, $F(x, E_p)$ is the neutrino spectra at each proton energy, and $x = E_\nu / E_p$. The neutrino production is first calculated at every radius from the star cluster and integrated over the

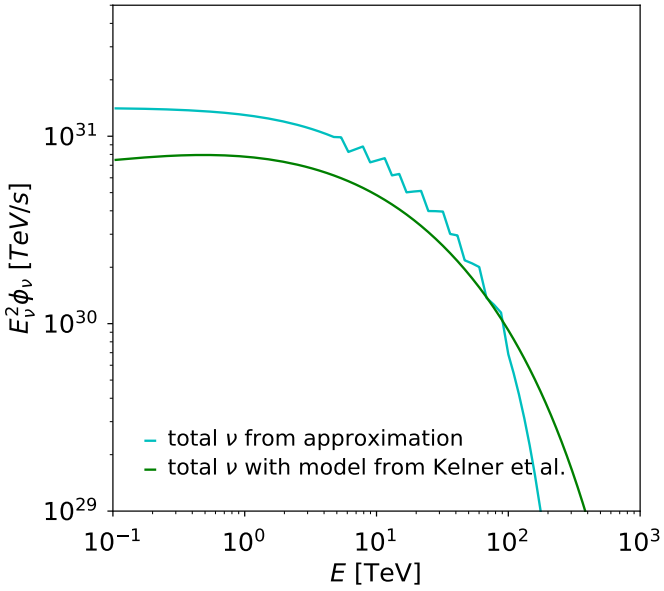

Figure 16: Prediction of neutrino production at the source estimated with two methods compared. The cyan line is estimated by considering the average values of neutrino energy and multiplicity. The green line is estimated with the model introduced in Kelner et al. (2006). The crinkled feature in the cyan line is a numerical effect due to the unevenly spaced energy grid.

whole volume of the emission region for scenario A and B. Furthermore, the more precise model of the p-p interaction cross section is adopted in this method [105]:

$$\sigma_{pp} = 34.3 + 1.88L + 0.25L^2 \quad \text{mb}, \tag{78}$$

where $L = \ln(E_p/1\text{TeV})$.

The comparison of neutrino production calculated based on the two estimation methods for the wind region (scenario A) under Bohm diffusion is shown in Fig. 16. The cyan line shows the estimation by assuming the average lab measured p-p interaction properties, and the green line shows the more precise calculation base on the model of Kelner et al. (2006). The two results are comparable in the order of magnitude but slightly differs in the spectra shapes.

5.1.3 *Result: Scenario A*

The total neutrino spectrum at the source calculated based on the CR phase space density obtained for scenario A under Bohm diffusion is shown in Fig.17. It is the neutrino production integrated over the volume of the wind bubble. From each production of charged pion, neutrinos of three flavors are with ratio (1:2:0) are expected. The total neutrino spectrum (the cyan line in Fig. 17) is calculated by adding up all flavors. From the CRs accelerated in the wind bubble, we have obtained up to $\sim$ 100 TeV neutrinos before the exponential cut-off. Fig. 18 compares the total neutrino production from CR spectra calculated under Bohm,

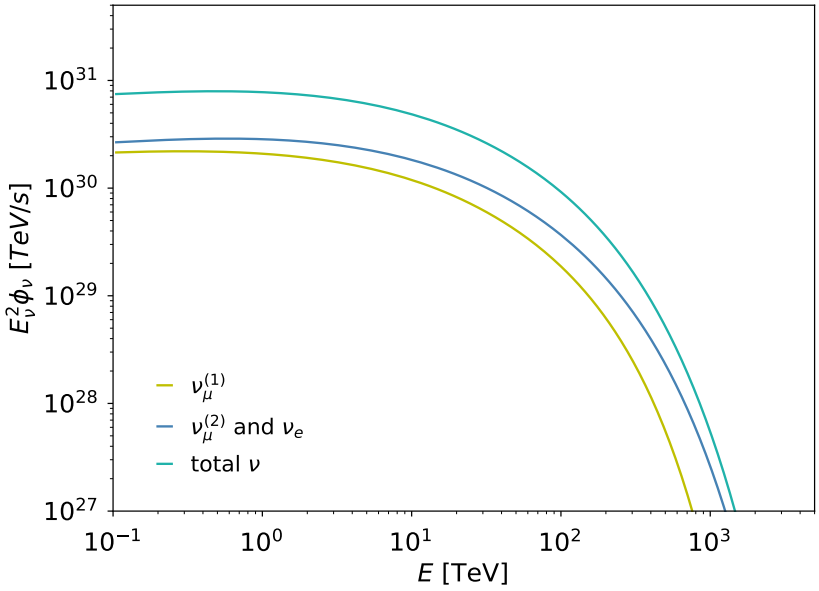

Figure 17: Neutrino production at the source integrated over the volume of the wind bubble under Bohm diffusion. The spectra show neutrino from pion decay (yellow), muon decay (blue), and the total production summed over all flavors (cyan).

Kraichnan, and Kolmogorov diffusion. Since CRs are accelerated to the highest energy under Bohm diffusion, we also obtain the highest energy neutrinos from p-p interaction. For Kraichnan diffusion, up to 10-100 TeV neutrinos are produced. While for Kolmogorov diffusion, neutrinos at 100 GeV are already exponentially suppressed due to the low cut-off of the CR spectrum. At 100 GeV, which is the lowest energy in the range of our consideration, we obtain the maximum neutrino production under Bohm in comparison to Kraichnan and Kolmogorov.

From the total neutrino production rate, the neutrino luminosity can be calculated for the three diffusion cases. Comparing the neutrino luminosity with the total wind luminosity $\sim 10^{38}$ TeV s^{-1}, we get an idea of the amount of energy budget transferred to neutrinos. The neutrino luminosity is calculated from:

$$L = \int dE_\nu \left(E_\nu \frac{dN_\nu}{dE_\nu dt} \right). \tag{79}$$

Among the three diffusion cases, Bohm diffusion results in the highest neutrino luminosity. The neutrino luminosity under Bohm diffusion is $\sim 8 \times 10^{31}$ TeV s^{-1}. For Kraichnan and Kolmogorov, the neutrino luminosities are $\sim 4 \times 10^{30}$ TeV s^{-1} and $\sim 10^{30}$ TeV s^{-1} respectively.

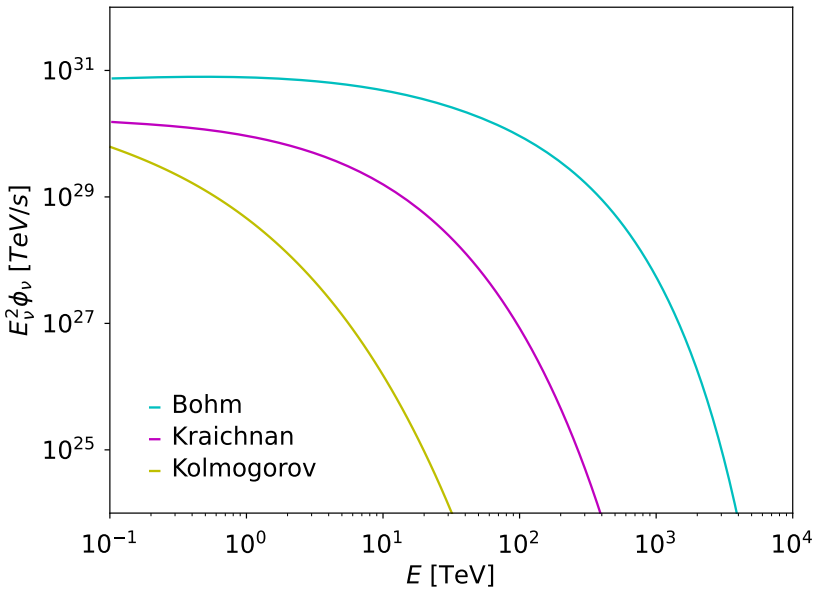

Figure 18: Scenario A: neutrino production integrated over the wind bubble at the source under Bohm (cyan), Karichnan (magenta), and Kolmogorov (yellow).

5.1.4 *Result: Scenario B*

In scenario B, not only the neutrinos produced in the wind bubble are studied, but also those produced in the thin layer of compressed ISM and the ambient ISM matter surrounding the wind bubble. The neutrino production in this case is integrated over each region separately to investigate the contribution to the total neutrino emission from a star cluster and its vicinity. Fig. 19 shows the total neutrino production under Bohm diffusion separating the contributions from the wind region (upstream and downstream of the wind bubble), the shocked ISM region, and the dense cloud region, which is the ambient ISM that we assume to span until 50 pc from the star cluster. The total neutrino produced at the source compared to scenario A under Bohm diffusion is around 3 orders of magnitude higher. The major contribution of the neutrino production is from the thin layer of compressed ISM in between the contact discontinuity and the forward shock. As shown in Fig. 14, the target mass density of the compressed ISM layer is the highest among all regions. Combined with the CR phase space in the compressed ISM region, p-p interaction happens the most frequently in this region, resulting in a dominant neutrino production. The interior of the wind bubble contribute the least to the total neutrino production. The neutrino production from the wind region is comparable to the total production predicted for scenario A, because the CR solution obtained in the wind region for scenario B is only slightly modified compared to scenario A.

The neutrino luminosity under Bohm diffusion at the source is $\sim 8 \times 10^{35}$ TeV s^{-1}, compared to $\sim 4 \times 10^{31}$ TeV s^{-1} under scenario A. The neutrino luminosity turns out to be a sizeable fraction $\sim$ 1% of the wind kinetic luminosity of $\sim 10^{38}$ TeV/s, therefore the dynamical impact of losses can be considered negligible. It is worth noting that, for ISM

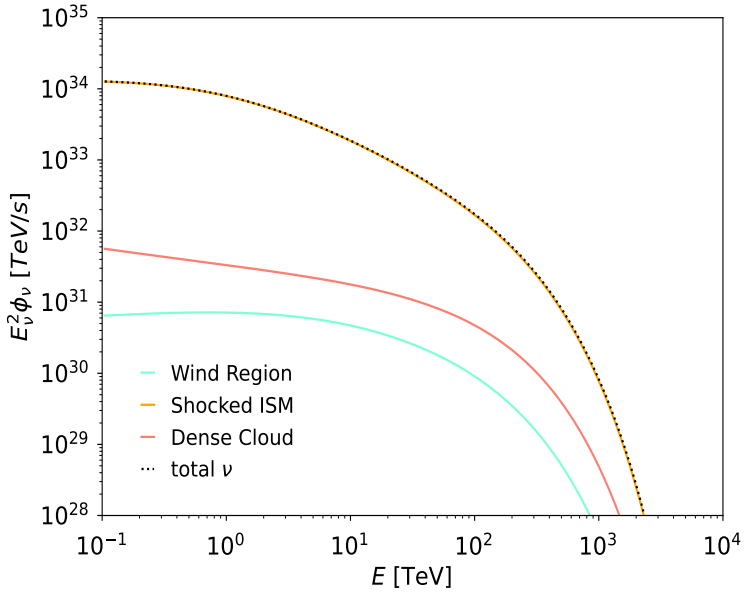

Figure 19: Scenario B: neutrino production at the source under Bohm diffusion: the contribution from each neutrino emission region are plotted. The lowest contribution is from the interior of the wind bubble (cyan). The shocked ISM dominates the production of neutrinos (pink).

with high density, the energy loss can become non-negligible, and affect the spectrum of accelerated particles as well as the flux of CRs released in the ISM.

The gamma-ray emission from p-p interaction at the source is also calculated based on the model introduced in Kelner et al. [105]. Fig. 20 shows the production of gamma-ray integrated over the whole emission regions and is compared with the total neutrino production. The gamma-ray spectra is similar to the neutrino spectra below TeV energy, and they start to diverge slightly from each other at higher energies.

5.2 GAMMA-RAY AND NEUTRINO FLUX AT EARTH

5.2.1 *Neutrino Flavor Oscillation*

In order to model the neutrinos from star clusters arriving at Earth and investigate the observational aspects by neutrino observatories. It is necessary to know the flavor content of the neutrinos and their flux. At the source, electron, muon, and pion neutrinos are produced at a rate of (1:2:0). However, this ratio changes as neutrinos travel from the source to the Earth. This property is called neutrino flavor oscillation.

The neutrino flavor oscillation is interpreted as a non-trival mixing of neutrino mass states and flavor states:

$$|\nu_\alpha\rangle = \sum_j U^*_{\alpha j} |v_j\rangle, \tag{80}$$

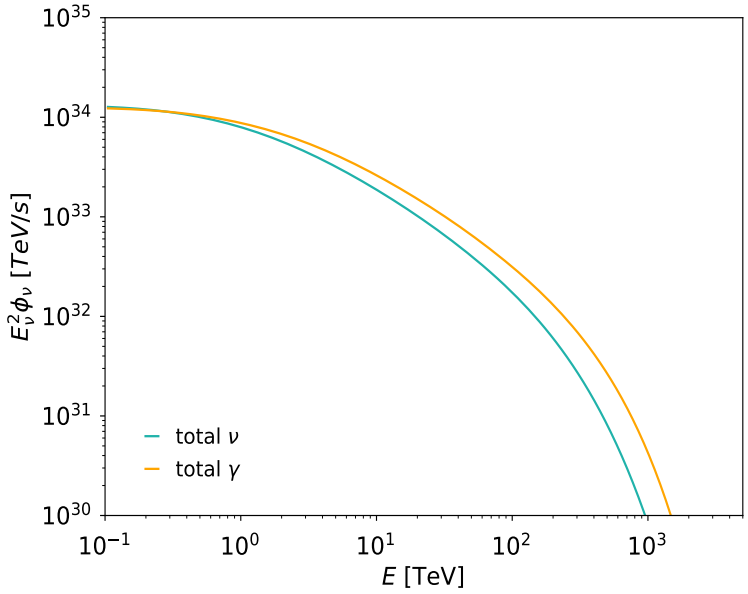

Figure 20: Total gamma-ray production (orange) for scenario B under Bohm diffusion integrated over all regions. The gamma-ray production is compared with the total neutrino production (blue). The difference of the two productions diverges slightly after a few TeV.

where $|\nu_\alpha\rangle$ is the neutrino flavor states with $\alpha = \mu, \pi, e$; $|\nu_j\rangle$ is the neutrino mass states with $j = 1, 2, 3$; and $U^*_{\alpha j}$ is the elements the Pontecorvo–Maki–Nakagawa–Sakata (PMNS) matrix. The PMNS matrix is unitary. It has dependence on three Euler rotation angles θ_{12},θ_{23} and θ_{13}, and the CP-violating phase δ:

$$U = \begin{pmatrix} 1 & 0 & 0 \\ 0 & c_{23} & c_{23} \\ 0 & -s_{23} & c_{23} \end{pmatrix} \begin{pmatrix} c_{13} & 0 & s_{13}e^{-i\delta} \\ 0 & 1 & 0 \\ -s_{13}e^{i\delta} & 0 & c_{13} \end{pmatrix} \begin{pmatrix} c_{12} & s_{12} & 0 \\ -s_{12} & c_{12} & 0 \\ 0 & 0 & 1 \end{pmatrix},$$

where s_{ij} and c_{ij} are abbreviations for $\sin\theta_{ij}$ and $\cos\theta_{ij}$. The neutrino flavor and mass states evolve as neutrinos travel a distance L, which corresponds to a time t ($L \approx ct$):

$$|\nu_\alpha(t)\rangle = \sum_j U^*_{\alpha j}|v_j(t)\rangle. \tag{81}$$

It can be solved with a plane wave solution, so that $|v_j(t)\rangle \simeq e^{\frac{-im_j^2 L}{2E}}|v_j(0)\rangle$. Given that a neutrino is flavor α at the source, its probability to oscillate to flavor β after traveling a distance L is $P_{\nu_\alpha\to\nu_\beta} = |\langle\nu_\beta|\nu_\alpha\rangle|^2$. Therefore, writing in terms of the mixing matrix elements, the probability of the flavor transition from α to β after a distance L is:

$$\langle P_{\nu_\alpha\to\nu_\beta}\rangle = \sum_{i=1}^{3}\sum_{j=1}^{3} U_{\alpha i}U^*_{\beta j}U^*_{\alpha j}U_{\beta}\langle e^{\left(\frac{i(m_i^2-m_j^2)L}{2E}\right)}\rangle. \tag{82}$$

	Normal Ordering (best fit)
$\theta_{12}/^\circ$	33.44
$\theta_{23}/^\circ$	49.2
$\theta_{13}/^\circ$	8.57
$\delta_{CP}/^\circ$	194

Table 3: The best fit values for the Euler rotation angles and CP-violation phase for normal mass ordering of neutrino flavor oscillation [107].

Over astronomical distances, the oscillation term becomes a random factor but for the case i=j, which means $\langle e^{\left(\frac{i(m_i^2-m_j^2)L}{2E}\right)}\rangle = \delta_{ij}$. Thus Eq. (82) can be rewritten as:

$$\langle P_{\nu_\alpha \to \nu_\beta} \rangle = \sum_{i=1}^{3} |U_{\alpha i}|^2 |U_{\beta i}|^2 \tag{83}$$

The oscillation-averaged flavor transition probability is calculated using Eq. (83) with the best fit parameter values listed in Table 3. Then we applied the oscillation probability matrix $\langle P_{\nu_\alpha \to \nu_\beta} \rangle$ to the neutrino flavor ratio (1:2:0) at the source to obtain the ratio we would expect over astrophysical distance. The result shows a ratio of (15:18:17) after oscillation, which is approximately (1:1:1).

Since neutrinos hardly interact when they propagate to the source to Earth, and the flavor oscillation does not affect the total flux of neutrinos, the neutrino spectra on Earth is simply related to the neutrino spectra at the source with a distance d as:

$$F_{\nu Earth} = \frac{\phi_{\nu_{source}}}{4\pi d^2}. \tag{84}$$

It can also be applied to gamma-ray flux estimations when the absorption is not significant.

5.2.2 *Result and discussion*

The investigation of the gamma-ray and neutrino productions at the source in Section 5.1 suggests that the compressed ISM region has a major contribution to the total neutrino production from a star cluster. While the contribution from the interior of the wind bubble is relatively insignificant. Since the complications in the setup of scenario B compared to scenario A are physical and substantial, scenario B is in favor of modeling gamma-ray and neutrino emissions from star clusters.

From the total gamma-ray production presented in Section 5.2 under scenario B (Fig. 20), the gamma-ray flux at Earth from Cygnus Cocoon and Westerlund 2 are estimated. The estimation is based on the same assumptions for the two systems of their wind velocity,

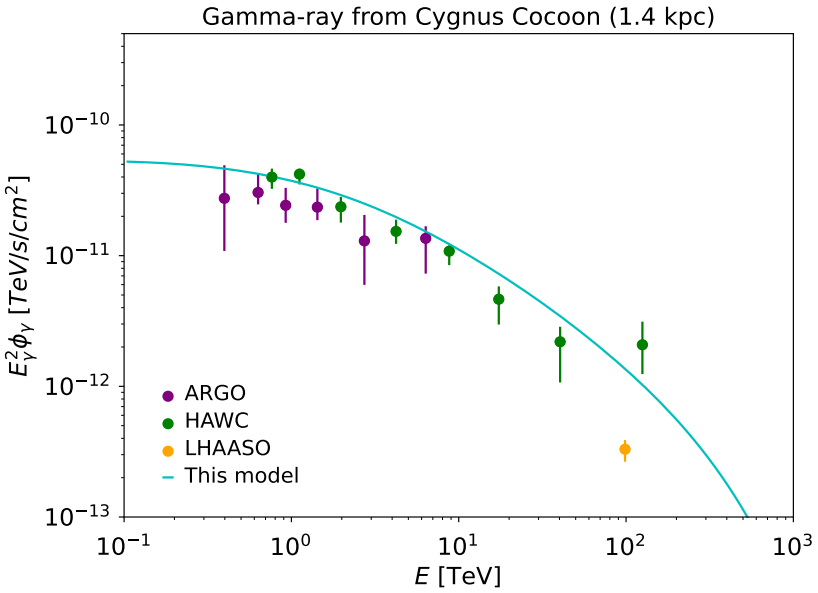

Figure 21: The model predicted gamma-ray flux (cyan line) at Earth from Cygnus Cocoon Compared with the observational data taken by ARGO (purple), HAWC (green), and LHAASO (yellow).

mass loss rate, and age of the two systems, which are consistent with the benchmark values used in the calculations above and are listed in Table 2. Therefore, only the distances from from the sources to Earth are varied. Eq. (84) is used for the estimation, which means the absorption of gamma-ray by starlight is not considered. Since the distances of Cygnus Cocoon ($\sim$1.4 kpc) and Westerlund 2 ($\sim$4 kpc) are close enough so that the absorption is not significant [108], the calculation is expected to provide a sensible estimation of the order of magnitude of gamma-ray flux expected from the sources. As mentioned in Chapter 3, Westerlund 2 and Cygnus Cocoon have been observed in GeV and TeV gamma-rays (e.g. [15, 66]). The expected gamma-ray flux calculated based on the model is compared to the observational data, which are shown in Fig. 21, and Fig. 22 for Cygnus Cocoon and Westerlund 2 respectively. The model describes the gamma-ray data quanlitatively under the assumption of a 3000 kms^{-1} wind speed, a 10^{-4} M$_\odot$ mass loss rate, an age of 1Myr, and the injection efficiency η_{in} tuned to the condition $P_{CR}|_{R_{sh}} = 5\% P_{ram}|_{R_{sh}}$. These parameters can be tuned to the specific systems to obtain a more accurate estimation of gamma-ray production. The consistency of the estimated gamma-ray flux with the observational data suggests that scenario B also leads to reasonable approximations of the neutrino flux. Other than the two sources we focus on in this project, the model can be also applied to other young massive star clusters for their gamma-ray and neutrino estimations.

Fig. 23 and Fig. 24 show the expected neutrino flux from Cygnus Cocoon and Westerlund 2 respectively. After the flavor oscillation as the neutrinos propagate from the star clusters to Earth, the three neutrino flavor ratio is close to $(1:1:1)$. The flux of each neutrino flavor becomes around 1/3 of the total neutrino flux arriving at Earth. TeV neutrino are

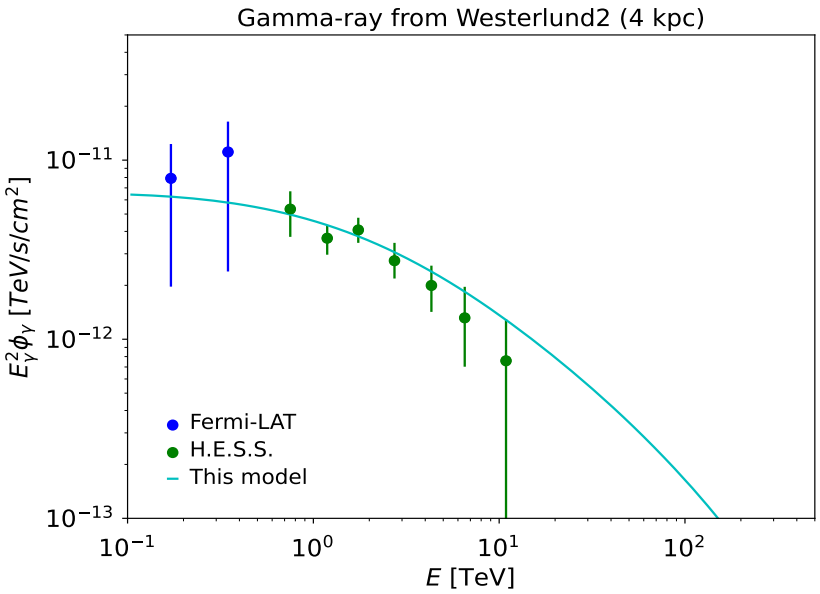

Figure 22: The model predicted gamma-ray flux (cyan line) at Earth from Westerlund 2 Compared with the observational data taken by Fermi-LAT (blue), and H.E.S.S. (green).

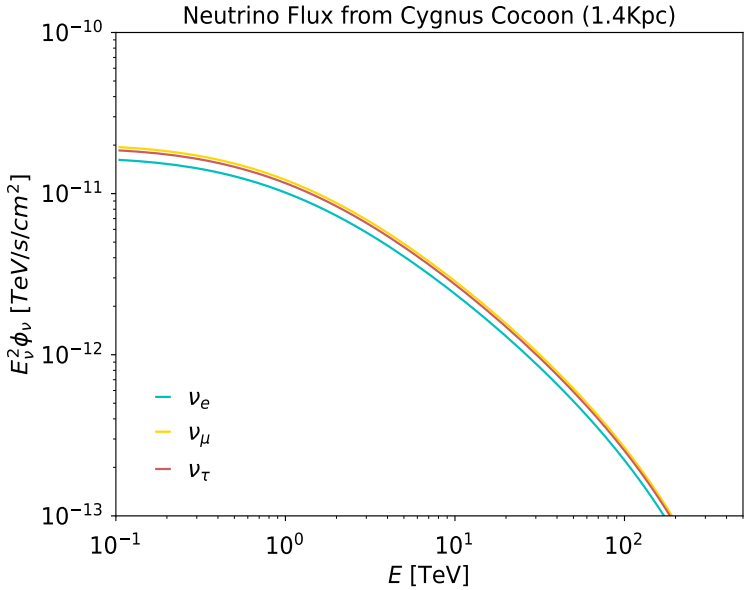

Figure 23: Neutrino flux expect on Earth calculated under scenario B from Cygnus Cocoon, which is located at 1.4kpc from the Earth. Each flavor of neutrino ν_μ,ν, and ν_τ after oscillation has comparable flux expected on Earth.

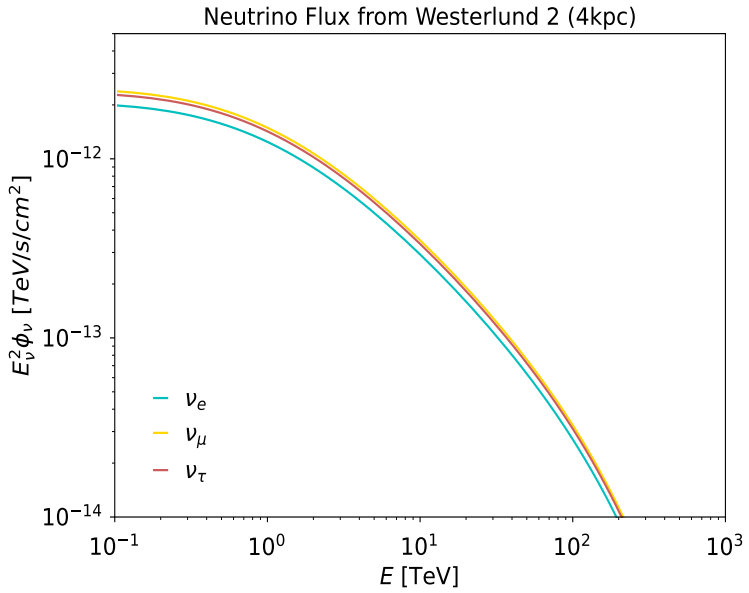

Figure 24: Neutrino flux expect on Earth calculated under scenario B from Westerlund 2, which is located at 4kpc from the Earth. Each flavor of neutrino ν_μ,ν, and ν_τ after oscillation has comparable flux expected on Earth.

expected to have a flux ϕ_ν of a few 10^{-11} TeV^{-1}s^{-1}cm^{-2} from Cygnus Cocoon and a few 10^{-12}TeV^{-1}s^{-1}cm^{-2} from Westerlund 2.

Based on the estimated neutrino flux at Earth, we aim to investigate the observational aspects of these sources by IceCube for potential detection. Fig. 25 shows the IceCube detection sensitivity of point-like sources and its dependencies on the declination δ of the source and the power-law index of the neutrino spectrum. The declinations of Cygnus Cocoon and Westerlund 2 are $\sim 40^\circ$ [12], and $\sim -57.5^\circ$ [14] respectively, corresponding to 0.64 and -0.84 in terms of $\sin(\delta)$. Above the detection threshold of IceCube of 100GeV, the estimated neutrino flux at is a few 10^{-11} TeV^{-1}s^{-1}cm^{-2} for Cygnus Cocoon (Fig. 23) and is a few 10^{-12} TeV^{-1}s^{-1}cm^{-2} for Westerlund 2 (Fig. 24). Since the estimated neutrino spectra exhibits a power-law index close to 3, we compare the estimated flux with the IceCube sensitivity for neutrino spectra of E^{-3}. The expected neutrino flux from Cygnus Cocoon is around the 90% detection sensitivity, while Westerlund 2 has an expected neutrino flux below the detection sensitivity. IceCube has a resolution of $\leq 1^\circ$ for track events at $\sim$TeV energy [109]. Cygnus Cocoon is located at a 1.4 kpc distance with a radius of $\sim$ 55 pc, which corresponds to an angular size of 2.1° [110]. Gamma-ray study of the vicinity of Westerlund 2 suggested that the dense cloud around Westerlund 2 has a radius of $\sim$ 210 pc [12], with a distance of 4 kpc, the angular size of the region is 3°. This means the observations of neutrinos from Cygnus Cocoon and Westerlund 2 are expected to be based on extended source detection instead of point sources. Nevertheless, future neutrino observatories, such as KM3NeT, can potentially detect Westerlund 2 and Cygnus Cocoon with a better sensitivity due to the observatory location and the new generation of instrument technology.

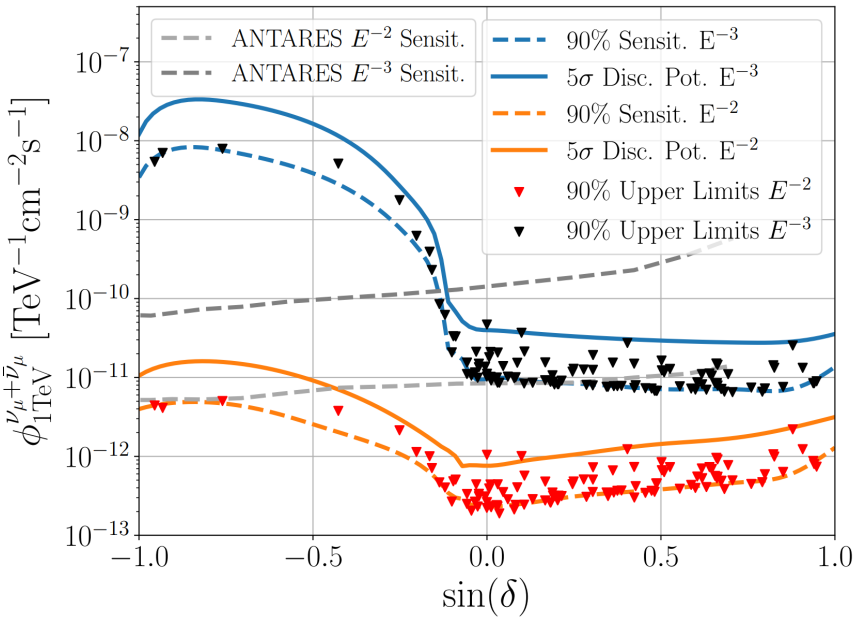

Figure 25: IceCube detection sensitivity based on the declination of the source and its neutrino flux: the sensitivity is shown for neutrino spectra of E^{-3} (blue) and E^{-2} (red). The sensitivity is compared with the medium sensitivity of ANTARES (gray) (plot is from [109]).

6

CONCLUSION AND OUTLOOK

We investigated young massive star cluster wind bubbles as candidate Galactic PeV-atron, and their multimessenger implications in terms of gamma-rays and neutrinos. Two setups of the systems were calculated and compared. Scenario A describes only the CRs in the interior of the wind bubble, while scenario B also includes CRs in the regions of the swept up ISM and the surrounding dense cloud. The phase space density inside of the wind bubble is slightly modified in the downstream of the wind and at the wind termination shock due to the change in the boundary condition at the forward shock. DSA at the wind termination shock under two scenarios leads to similar CR spectra at R_{sh} with an unnoticeable difference. The maximum energies of the acceleration under the two scenarios are nearly the same. Bohm diffusion of CRs leads to the most efficient acceleration in the wind bubble. A star cluster wind bubble with a wind speed of 3000kms^{-1} and a mass loss rate of 10^{-4} M$_{\odot}$ is efficient to accelerate particles to PeV energies. Thus, star cluster wind bubbles are plausible sources of GCRs up to the 'knee'.

The p-p interaction of the accelerated charged particles with matter inside the wind bubble and in the ISM result in the source shining in gamma-rays and neutrinos. The two scenarios give comparable results for neutrino production in the interior of the wind bubble. The neutrino luminosity from the wind region, which is the total neutrino luminosity under scenario A, is at a relatively low level of $10^{31} - 10^{32}$ TeV s^{-1}. On the other hand, we find that the layer of compressed ISM introduced in scenario B is the major contributor to the total neutrino production. The neutrino luminosity after including the compressed ISM and the ambient ISM regions reaches a level of $\sim 10^{36}$TeVs^{-1}. Therefore, the configuration of scenario B is more efficient in neutrino production from the source.

The neutrino and gamma-ray fluxes expected at Earth from two nearby star clusters: Cygnus Cocoon and Westerlund 2, are estimated based on their distances from Earth. The estimated gamma-ray flux is compared with observational data from a series of observations of the two star clusters. The estimation agrees qualitatively with the observational data for, both, Cygnus Cocoon and Westerlund 2. Therefore, we suggest that the neutrino fluxes estimated from the two sources provide a prediction for potential neutrino observations. The estimated neutrino flux from Cygnus Cocoon is close to the sensitivity for point-like sources detection

of IceCube, while Westerlund 2 has a flux beyond the reach of IceCube. However, the angular sizes of both of the two sources extend $> 1^{\circ}$. Based on the IceCube resolution, the observation of Cygnus Cocoon and Westerlund 2 need to be based on the analysis of extended source detection.

One free parameter of the model is the ratio of the CR pressure to the wind ram pressure at the wind termination shock. The particle injection efficiency η_{in} is determined to assure a ratio of $P_{CR}/P_{ram} = 5\%$ at the shock front in order to insure a test particle regime of the system. The ratio can be adjusted within the range where CRs do not have a significant impact on the structure of the wind bubble and the acceleration scheme. In future studies, the model can be extended to investigate the scenarios when the test particle regime is violated.

The gamma-ray and neutrino fluxes from Cygnus Cocoon and Westerlund 2 presented in this work are calculated based on the same assumptions of the benchmark values of the wind velocity, mass loss rate, and the age of the systems. These values can be tuned based on the specific systems to obtain more precise estimations of the fluxes. Furthermore, the gamma-ray fluxes estimated at Earth from the two sources are calculated without considering the absorption effect of gamma-rays on starlight during the propagation from the source to Earth. Therefore, including the absorption effect in gamma-ray estimation leads to better comparisons with the observational data of the sources. Last but not the least, the relativistic electrons co-accelerated in the system with CRs and from the charged pion decay result in gamma-rays via Bremsstrahlung and Inverse Compton emission. The model thus can be further explored with the electrons in the system.

BIBLIOGRAPHY

[1] Victor Hess. *On the Observations of the Penetrating Radiation during Seven Balloon Flights*. 2018. DOI: 10.48550/ARXIV.1808.02927. URL: https://arxiv.org/abs/1808.02927.

[2] Jörg R. Höorandel. "A review of experimental results at the knee". In: *Journal of Physics Conference Series*. Vol. 47. Journal of Physics Conference Series. Oct. 2006, pp. 41–50. DOI: 10.1088/1742-6596/47/1/005. arXiv: astro-ph/0508014 [astro-ph].

[3] V. L. Ginzburg and S. I. Syrovatskii. *The Origin of Cosmic Rays*. 1964.

[4] W. I. Axford. "The acceleration of galactic cosmic rays". In: *Origin of Cosmic Rays*. Ed. by G. Setti, G. Spada, and A. W. Wolfendale. Vol. 94. Jan. 1981, pp. 339–358.

[5] S. P. Reynolds. "Supernova remnants at high energy." In: 46 (Sept. 2008), pp. 89–126. DOI: 10.1146/annurev.astro.46.060407.145237.

[6] P. O. Lagage and C. J. Cesarsky. "The maximum energy of cosmic rays accelerated by supernova shocks." In: 125 (Sept. 1983), pp. 249–257.

[7] P. Cristofari, P. Blasi, and D. Caprioli. "Cosmic ray protons and electrons from supernova remnants". In: *Astron. Astrophys.* 650 (2021), A62. DOI: 10.1051/0004-6361/202140448. arXiv: 2103.02375 [astro-ph.HE].

[8] Felix Aharonian, Ruizhi Yang, and Emma de Oña Wilhelmi. *Massive Stars as Major Factories of Galactic Cosmic Rays*. 2018. DOI: 10.48550/ARXIV.1804.02331. URL: https://arxiv.org/abs/1804.02331.

[9] E. Parizot et al. "Superbubbles and energetic particles in the Galaxy". In: *Astronomy &amp Astrophysics* 424.3 (Sept. 2004), pp. 747–760. DOI: 10.1051/0004-6361:20041269. URL: https://doi.org/10.1051%2F0004-6361%3A20041269.

[10] Andrei M. Bykov. "Nonthermal particles and photons in starburst regions and superbubbles". In: *The Astronomy and Astrophysics Review* 22.1 (Oct. 2014). DOI: 10.1007/s00159-014-0077-8. URL: https://doi.org/10.1007%2Fs00159-014-0077-8.

[11] Rui-zhi Yang, Felix Aharonian, and Emma de Oña Wilhelmi. "Massive star clusters as the an alternative source population of galactic cosmic rays". In: *Rendiconti Lincei. Scienze Fisiche e Naturali* 30 (Dec. 2019), pp. 159–164. DOI: 10.1007/s12210-019-00819-3.

[12] Rui-zhi Yang, Emma de Oñ a Wilhelmi, and Felix Aharonian. “Diffuse i/i-ray emission in the vicinity of young star cluster Westerlund 2”. In: *Astronomy &amp Astrophysics* 611 (Mar. 2018), A77. DOI: 10.1051/0004-6361/201732045. URL: https://doi.org/10.1051%2F0004-6361%2F201732045.

[13] A. Abramowski et al. “Discovery of extended VHEi/i-ray emission from the vicinity of the young massive stellar cluster Westerlund 1”. In: *Astronomy &amp Astrophysics* 537 (Jan. 2012), A114. DOI: 10.1051/0004-6361/201117928. URL: https://doi.org/10.1051%2F0004-6361%2F201117928.

[14] H. E. S. S. Collaboration et al. “Revisiting the Westerlund 2 field with the HESS telescope array”. In: 525, A46 (Jan. 2011), A46. DOI: 10.1051/0004-6361/201015290. arXiv: 1009.3012 [astro-ph.HE].

[15] Markus Ackermann et al. “A cocoon of freshly accelerated cosmic rays detected by Fermi in the Cygnus superbubble”. In: *science* 334.6059 (2011), pp. 1103–1107.

[16] B. Bartoli et al. “IDENTIFICATION OF THE TeV GAMMA-RAY SOURCE ARGO J20314157 WITH THE CYGNUS COCOON”. In: *The Astrophysical Journal* 790.2 (July 2014), p. 152. DOI: 10.1088/0004-637x/790/2/152. URL: https://doi.org/10.1088%2F0004-637x%2F790%2F2%2F152.

[17] Rui-zhi Yang and Felix Aharonian. “Diffuse γ-ray emission near the young massive cluster NGC 3603”. In: 600, A107 (Apr. 2017), A107. DOI: 10.1051/0004-6361/201630213. arXiv: 1612.02250 [astro-ph.HE].

[18] G Morlino et al. “Particle acceleration in winds of star clusters”. In: *Monthly Notices of the Royal Astronomical Society* 504.4 (Mar. 2021), pp. 6096–6105. ISSN: 1365-2966. DOI: 10.1093/mnras/stab690. URL: http://dx.doi.org/10.1093/mnras/stab690.

[19] Malcolm S. Longair. *High Energy Astrophysics*. 3rd ed. Cambridge University Press, 2011. DOI: 10.1017/CBO9780511778346.

[20] L. A. Fisk. “Solar modulation of galactic cosmic rays”. In: *The Ancient Sun: Fossil Record in the Earth, Moon and Meteorites*. Ed. by R. O. Pepin, J. A. Eddy, and R. B. Merrill. Jan. 1980, pp. 103–118.

[21] M. Amenomori et al. “The All-Particle Spectrum of Primary Cosmic Rays in the Wide Energy Range from 10sup14/supto 10sup17/supeV Observed with the Tibet-III Air-Shower Array”. In: *The Astrophysical Journal* 678.2 (May 2008), pp. 1165–1179. DOI: 10.1086/529514. URL: https://doi.org/10.1086%2F529514.

[22] J. Abraham et al. “Measurement of the energy spectrum of cosmic rays above 1018 eV using the Pierre Auger Observatory”. In: *Physics Letters B* 685.4-5 (Mar. 2010), pp. 239–246. DOI: 10.1016/j.physletb.2010.02.013. URL: https://doi.org/10.1016%2Fj.physletb.2010.02.013.

[23] Carmelo Evoli. *The Cosmic-Ray Energy Spectrum*. Dec. 2020. DOI: 10.5281/zenodo.4396125. URL: https://doi.org/10.5281/zenodo.4396125.

[24] V. S. Ptuskin et al. "Diffusion and drift of very high energy cosmic rays in galactic magnetic fields". In: 268.2 (Feb. 1993), pp. 726–735.

[25] Joerg Rudolf Hoerandel, N. N. Kalmykov, and A. I. Pavlov. "The Knee in the Energy Spectrum of Cosmic Rays in the Framework of the Poly-Gonato and Diffusion Models". In: *International Cosmic Ray Conference*. Vol. 1. International Cosmic Ray Conference. July 2003, p. 243.

[26] Esteban Roulet. "Astroparticle theory: Some new insights into high energy cosmic rays". In: *International Journal of Modern Physics A* 19.07 (2004), pp. 1133–1141.

[27] K. Boothby et al. "A New Measurement of Cosmic-Ray Composition at the Knee". In: *The Astrophysical Journal* 491.1 (Dec. 1997), pp. L35–L38. DOI: 10.1086/311049. URL: https://doi.org/10.1086/311049.

[28] A.A. Lagutin, Yu.A. Nikulin, and V.V. Uchaikin. "The "knee" in the primary cosmic ray spectrum as consequence of the anomalous diffusion of the particles in the fractal interstellar medium". In: *Nuclear Physics B - Proceedings Supplements* 97.1 (2001), pp. 267–270. ISSN: 0920-5632. DOI: https://doi.org/10.1016/S0920-5632(01)01280-4. URL: https://www.sciencedirect.com/science/article/pii/S0920563201012804.

[29] E. G. Berezhko and L. T. Ksenofontov. "Cosmic Rays, Radio and Gamma-Ray Emission from the Remnant of Supernova 1987A". In: *Astronomy Letters* 26.10 (Oct. 2000), pp. 639–656. DOI: 10.1134/1.1316109.

[30] T. Stanev, P. L. Biermann, and T. K. Gaisser. "Cosmic rays. IV. The spectrum and chemical composition above 10' GeV". In: 274 (July 1993), p. 902. arXiv: astro-ph/9303006 [astro-ph].

[31] K. Kobayakawa, Y. Sato, and T. Samura. "Acceleration of particles by oblique shocks and cosmic ray spectra around the knee region". In: *Phys. Rev. D* 66 (2002), p. 083004. DOI: 10.1103/PhysRevD.66.083004. arXiv: astro-ph/0008209.

[32] Lyubov G Sveshnikova. "The knee in the Galactic cosmic ray spectrum and variety in Supernovae". In: *Astronomy & Astrophysics* 409.3 (2003), pp. 799–807.

[33] A. D. Erlykin and A. W. Wolfendale. "Supernova remnants and the origin of the cosmic radiation. III: Spectral differences for different nuclei". In: *J. Phys. G* 27 (2001), pp. 1709–1721. DOI: 10.1088/0954-3899/27/8/301.

[34] M. Aglietta et al. "Measurement of the cosmic ray hadron spectrum up to 30 TeV at mountain altitude: the primary proton spectrum". In: *Astroparticle Physics* 19.3 (2003), pp. 329–338. ISSN: 0927-6505. DOI: https://doi.org/10.1016/S0927-6505(03)00103-8. URL: https://www.sciencedirect.com/science/article/pii/S0927650503001038.

[35] T. Antoni et al. “The Primary Proton Spectrum of Cosmic Rays Measured with Single Hadrons at Ground Level”. In: *The Astrophysical Journal* 612.2 (Sept. 2004), pp. 914–920. DOI: 10.1086/422674. URL: https://doi.org/10.1086/422674.

[36] Pasquale Blasi. “The origin of galactic cosmic rays”. In: *The Astronomy and Astrophysics Review* 21.1 (Nov. 2013). DOI: 10.1007/s00159-013-0070-7. URL: https://doi.org/10.1007%2Fs00159-013-0070-7.

[37] A. M. Hillas. “TOPICAL REVIEW: Can diffusive shock acceleration in supernova remnants account for high-energy galactic cosmic rays?” In: *Journal of Physics G Nuclear Physics* 31.5 (May 2005), R95–R131. DOI: 10.1088/0954-3899/31/5/R02.

[38] Tadeusz Wibig and Arnold W. Wolfendale. “At what particle energy do extragalactic cosmic rays start to predominate?” In: (2004). DOI: 10.48550/ARXIV.ASTRO-PH/0410624. URL: https://arxiv.org/abs/astro-ph/0410624.

[39] Rainer Beck. “Magnetic Fields in Galaxies”. In: *Space Sciences Series of ISSI*. Springer New York, 2011, pp. 215–230. DOI: 10.1007/978-1-4614-5728-2_8. URL: https://doi.org/10.1007%2F978-1-4614-5728-2_8.

[40] Gregory Dobler et al. “THEiFERMI/iHAZE: A GAMMA-RAY COUNTERPART TO THE MICROWAVE HAZE”. In: *The Astrophysical Journal* 717.2 (June 2010), pp. 825–842. DOI: 10.1088/0004-637x/717/2/825. URL: https://doi.org/10.1088%2F0004-637x%2F717%2F2%2F825.

[41] Federico Abbate et al. “Constraints on the magnetic field in the Galactic halo from globular cluster pulsars”. In: *Nature Astronomy* 4.7 (Mar. 2020), pp. 704–710. DOI: 10.1038/s41550-020-1030-6. URL: https://doi.org/10.1038%2Fs41550-020-1030-6.

[42] Luke O’C. Drury. “Origin of cosmic rays”. In: *Astroparticle Physics* 39-40 (Dec. 2012), pp. 52–60. DOI: 10.1016/j.astropartphys.2012.02.006. URL: https://doi.org/10.1016%2Fj.astropartphys.2012.02.006.

[43] Matt Nicholl et al. “An extremely energetic supernova from a very massive star in a dense medium”. In: *Nature Astronomy* 4.9 (Apr. 2020), pp. 893–899. DOI: 10.1038/s41550-020-1066-7. URL: https://doi.org/10.1038%2Fs41550-020-1066-7.

[44] Roger Blandford and David Eichler. “Particle acceleration at astrophysical shocks: A theory of cosmic ray origin”. In: *Physics Reports* 154.1 (1987), pp. 1–75. ISSN: 0370-1573. DOI: https://doi.org/10.1016/0370-1573(87)90134-7. URL: https://www.sciencedirect.com/science/article/pii/0370157387901347.

[45] A. M. Bykov et al. “Cosmic Ray Production in Supernovae”. In: *Space Science Reviews* 214.1 (Jan. 2018). DOI: 10.1007/s11214-018-0479-4. URL: https://doi.org/10.1007%2Fs11214-018-0479-4.

[46] G. A. Tammann, W. Loeffler, and A. Schroeder. “The Galactic Supernova Rate”. In: 92 (June 1994), p. 487. DOI: 10.1086/192002.

[47] N. E. Yanasak et al. “Measurement of the Secondary Radionuclides ^{10}Be, ^{26}Al, ^{36}Cl, ^{54}Mn, and ^{14}C and Implications for the Galactic Cosmic-Ray Age”. In: *The Astrophysical Journal* 563.2 (Dec. 2001), pp. 768–792. DOI: 10.1086/323842. URL: https://doi.org/10.1086/323842.

[48] E. A. Helder et al. “Observational Signatures of Particle Acceleration in Supernova Remnants”. In: *Space Science Reviews* 173.1-4 (Aug. 2012), pp. 369–431. DOI: 10.1007/s11214-012-9919-8. URL: https://doi.org/10.1007%2Fs11214-012-9919-8.

[49] M. Ackermann et al. “Detection of the Characteristic Pion-Decay Signature in Supernova Remnants”. In: *Science* 339.6121 (2013), pp. 807–811. DOI: 10.1126/science.1231160. eprint: https://www.science.org/doi/pdf/10.1126/science.1231160. URL: https://www.science.org/doi/abs/10.1126/science.1231160.

[50] A. I. Asvarov. “Radio emission from shell-type supernova remnants”. In: 459.2 (Nov. 2006), pp. 519–533. DOI: 10.1051/0004-6361:20041155. arXiv: astro-ph/0608079 [astro-ph].

[51] F. A. Aharonian et al. “High-energy particle acceleration in the shell of a supernova remnant”. In: *Nature* 432.7013 (Nov. 2004), pp. 75–77. DOI: 10.1038/nature02960. URL: https://doi.org/10.1038%2Fnature02960.

[52] F. Aharonian et al. “H.E.S.S. Observations of the Supernova Remnant RX J0852.0-4622: Shell-Type Morphology and Spectrum of a Widely Extended Very High Energy Gamma-Ray Source”. In: *The Astrophysical Journal* 661.1 (May 2007), pp. 236–249. DOI: 10.1086/512603. URL: https://doi.org/10.1086/512603.

[53] and A. Abramowski et al. “A new SNR with TeV shell-type morphology: HESS J1731-347”. In: *Astronomy &amp Astrophysics* 531 (June 2011), A81. DOI: 10.1051/0004-6361/201016425. URL: https://doi.org/10.1051%2F0004-6361%2F201016425.

[54] F. Aharonian et al. “DISCOVERY OF GAMMA-RAY EMISSION FROM THE SHELL-TYPE SUPERNOVA REMNANT RCW 86 WITH HESS”. In: *The Astrophysical Journal* 692.2 (Feb. 2009), pp. 1500–1505. DOI: 10.1088/0004-637x/692/2/1500. URL: https://doi.org/10.1088%2F0004-637x%2F692%2F2%2F1500.

[55] F. Acero et al. “First detection of VHE gamma-rays from SN 1006 by H.E.S.S”. In: *Astron. Astrophys.* 516 (2010), A62. DOI: 10.1051/0004-6361/200913916. arXiv: 1004.2124 [astro-ph.HE].

[56] S. G. Lucek and A. R. Bell. “Non-linear amplification of a magnetic field driven by cosmic ray streaming”. In: *Monthly Notices of the Royal Astronomical Society* 314.1 (2000), pp. 65–74. DOI: https://doi.org/10.1046/j.1365-8711.2000.03363.x. eprint: https://onlinelibrary.wiley.com/doi/pdf/10.1046/j.1365-8711.2000.03363.x. URL: https://onlinelibrary.wiley.com/doi/abs/10.1046/j.1365-8711.2000.03363.x.

[57] Mark R. Krumholz, Christopher F. McKee, and Joss Bland-Hawthorn. “Star Clusters Across Cosmic Time”. In: *Annual Review of Astronomy and Astrophysics* 57.1 (2019), pp. 227–303. DOI: 10.1146/annurev-astro-091918-104430. eprint: https://doi.org/10.1146/annurev-astro-091918-104430. URL: https://doi.org/10.1146/annurev-astro-091918-104430.

[58] NASA. *Westerlund2 image by Space Telescope and Chandra*. 2016. URL: https://www.nasa.gov/mission_pages/chandra/discovering-the-treasures-in-chandra-s-archives.html (visited on 10/14/2016).

[59] J. P. Simpson. “IRS Observations of PAHs and CO_2 Ice in the Galactic Center”. In: *The Evolving ISM in the Milky Way and Nearby Galaxies*. Ed. by K. Sheth et al. Jan. 2009, 60, p. 60.

[60] NASA. *Quintuplet image by Hubble-Spitzer*. 2009. URL: https://esahubble.org/images/opo0902d/ (visited on 01/05/2009).

[61] I. R. Stevens and J. M. Hartwell. “The Cluster Wind from Young Massive Star Clusters”. In: *The Formation and Evolution of Massive Young Star Clusters*. Ed. by Henry J. G. L. M. Lamers, Linda J. Smith, and Antonella Nota. Vol. 322. Astronomical Society of the Pacific Conference Series. Dec. 2004, p. 169.

[62] G. M. Webb, W. I. Axford, and M. A. Forman. “Cosmic-ray acceleration at stellar wind terminal shocks”. In: 298 (Nov. 1985), pp. 684–709. DOI: 10.1086/163652.

[63] Siddhartha Gupta, Biman B Nath, and Prateek Sharma. “Constraining cosmic ray acceleration in young star clusters using multi-wavelength observations”. In: *Monthly Notices of the Royal Astronomical Society* 479.4 (July 2018), pp. 5220–5234. ISSN: 0035-8711. DOI: 10.1093/mnras/sty1846. eprint: https://academic.oup.com/mnras/article-pdf/479/4/5220/25207726/sty1846.pdf. URL: https://doi.org/10.1093/mnras/sty1846.

[64] Simon F. Portegies Zwart, Stephen L.W. McMillan, and Mark Gieles. "Young Massive Star Clusters". In: *Annual Review of Astronomy and Astrophysics* 48.1 (2010), pp. 431–493. DOI: 10.1146/annurev-astro-081309-130834. eprint: https://doi.org/10.1146/annurev-astro-081309-130834. URL: https://doi.org/10.1146/annurev-astro-081309-130834.

[65] H. E. S. S. Collaboration et al. "The exceptionally powerful TeV γ-ray emitters in the Large Magellanic Cloud". In: *Science* 347.6220 (Jan. 2015), pp. 406–412. DOI: 10.1126/science.1261313. arXiv: 1501.06578 [astro-ph.HE].

[66] Aharonian, F. et al. "Detection of extended very-high-energy emission towards the young stellar cluster Westerlund 2". In: *A&A* 467.3 (2007), pp. 1075–1080. DOI: 10.1051/0004-6361:20066950. URL: https://doi.org/10.1051/0004-6361:20066950.

[67] Martin Israel. *An Overview of Cosmic-Ray Elemental Composition*. 2004. URL: https://izw1.caltech.edu/ACE/ACENews/ACENews83.html (visited on 09/30/2010).

[68] G.W. Adams and A.J. Masley. "Production rates and electron densities in the lower ionosphere due to solar cosmic rays". In: *Journal of Atmospheric and Terrestrial Physics* 27.3 (1965), pp. 289–298. ISSN: 0021-9169. DOI: https://doi.org/10.1016/0021-9169(65)90029-2. URL: https://www.sciencedirect.com/science/article/pii/0021916965900292.

[69] Floyd William Stecker. *Cosmic gamma rays*. Vol. 249. 1971.

[70] D. Eichler. "High-energy neutrino astronomy: a probe of galactic nuclei?" In: 232 (Aug. 1979), pp. 106–112. DOI: 10.1086/157269.

[71] Maurizio Spurio, Spurio, and Bellantone. *Probes of Multimessenger Astrophysics*. Springer, 2018.

[72] Thomas K. Gaisser. *Cosmic rays and particle physics.* 1990.

[73] Péter Mészáros et al. "Multi-messenger astrophysics". In: *Nature Reviews Physics* 1.10 (Oct. 2019), pp. 585–599. DOI: 10.1038/s42254-019-0101-z. URL: https://doi.org/10.1038%2Fs42254-019-0101-z.

[74] Luigi Tibaldo, Daniele Gaggero, and Pierrick Martin. "Gamma Rays as Probes of Cosmic-Ray Propagation and Interactions in Galaxies". In: *Universe* 7.5 (May 2021), p. 141. DOI: 10.3390/universe7050141. URL: https://doi.org/10.3390%2Funiverse7050141.

[75] W. B. Atwood et al. "THE LARGE AREA TELESCOPE ON THEiFERMI GAMMA-RAY SPACE TELESCOPE/iMISSION". In: *The Astrophysical Journal* 697.2 (May 2009), pp. 1071–1102. DOI: 10.1088/0004-637x/697/2/1071. URL: https://doi.org/10.1088%2F0004-637x%2F697%2F2%2F1071.

[76] Mathieu de Naurois and Daniel Mazin. “Ground-based detectors in very-high-energy gamma-ray astronomy”. In: *Comptes Rendus Physique* 16.6-7 (Aug. 2015), pp. 610–627. DOI: 10.1016/j.crhy.2015.08.011. URL: https://doi.org/10.1016%2Fj.crhy.2015.08.011.

[77] A. Karle. *IceCube*. 2010. DOI: 10.48550/ARXIV.1003.5715. URL: https://arxiv.org/abs/1003.5715.

[78] Dmitry Chirkin and Wolfgang Rhode. *Propagating leptons through matter with Muon Monte Carlo (MMC)*. 2004. DOI: 10.48550/ARXIV.HEP-PH/0407075. URL: https://arxiv.org/abs/hep-ph/0407075.

[79] Markus Ahlers, Klaus Helbing, and Carlos Pérez de los Heros. “Probing particle physics with IceCube”. In: *The European Physical Journal C* 78.11 (Nov. 2018). DOI: 10.1140/epjc/s10052-018-6369-9. URL: https://doi.org/10.1140%2Fepjc%2Fs10052-018-6369-9.

[80] M. G. Aartsen et al. “Search for Astrophysical Sources of Neutrinos Using Cascade Events in IceCube”. In: *The Astrophysical Journal* 846.2 (Sept. 2017), p. 136. DOI: 10.3847/1538-4357/aa8508. URL: https://doi.org/10.3847%2F1538-4357%2Faa8508.

[81] W. I. Axford, E. Leer, and G. Skadron. “The Acceleration of Cosmic Rays by Shock Waves”. In: *International Cosmic Ray Conference*. Vol. 11. International Cosmic Ray Conference. Jan. 1977, p. 132.

[82] G. F. Krymskii. “A regular mechanism for the acceleration of charged particles on the front of a shock wave”. In: *Akademiia Nauk SSSR Doklady* 234 (June 1977), pp. 1306–1308.

[83] A. R. Bell. “The acceleration of cosmic rays in shock fronts - I.” In: 182 (Jan. 1978), pp. 147–156. DOI: 10.1093/mnras/182.2.147.

[84] R. D. Blandford and J. P. Ostriker. “Particle acceleration by astrophysical shocks.” In: 221 (Apr. 1978), pp. L29–L32. DOI: 10.1086/182658.

[85] J. Skilling. “Cosmic Ray Streaming—I Effect of Alfvén Waves on Particles”. In: *Monthly Notices of the Royal Astronomical Society* 172.3 (Sept. 1975), pp. 557–566. ISSN: 0035-8711. DOI: 10.1093/mnras/172.3.557. eprint: https://academic.oup.com/mnras/article-pdf/172/3/557/2927415/mnras172-0557.pdf. URL: https://doi.org/10.1093/mnras/172.3.557.

[86] L O’C Drury. “An introduction to the theory of diffusive shock acceleration of energetic particles in tenuous plasmas”. In: *Reports on Progress in Physics* 46.8 (Aug. 1983), pp. 973–1027. DOI: 10.1088/0034-4885/46/8/002. URL: https://doi.org/10.1088/0034-4885/46/8/002.

[87] M. Fatuzzo and F. Melia. "A NUMERICAL ASSESSMENT OF COSMIC-RAY ENERGY DIFFUSION THROUGH TURBULENT MEDIA". In: *The Astrophysical Journal* 784.2 (Mar. 2014), p. 131. DOI: 10.1088/0004-637x/784/2/131. URL: https://doi.org/10.1088%2F0004-637x%2F784%2F2%2F131.

[88] Günter Sigl. "Astroparticle Physics: Theory and Phenomenology". In: (2017).

[89] J. T. Gosling et al. "Satellite observations of interplanetary shock waves". In: *Journal of Geophysical Research (1896-1977)* 73.1 (1968), pp. 43–50. DOI: https://doi.org/10.1029/JA073i001p00043. eprint: https://agupubs.onlinelibrary.wiley.com/doi/pdf/10.1029/JA073i001p00043. URL: https://agupubs.onlinelibrary.wiley.com/doi/abs/10.1029/JA073i001p00043.

[90] J. R. Jokipii. "Acceleration and Transport Processes - Verification and Observations". In: 36.1 (Sept. 1983), pp. 27–40. DOI: 10.1007/BF00171898.

[91] Donald C. Ellison et al. "Supernova Remnants and the Physics of Strong Shock Waves". In: *Publications of the Astronomical Society of the Pacific* 106.701 (1994), pp. 780–797. ISSN: 00046280, 15383873. URL: http://www.jstor.org/stable/40680428 (visited on 05/21/2022).

[92] S. A. Lamzin. "The Structure of Shock Waves in the Case of Accretion onto Low-Mass Young Stars". In: (2013). DOI: 10.48550/ARXIV.1303.4066. URL: https://arxiv.org/abs/1303.4066.

[93] C. F. Kennel and F. V. Coroniti. "Magnetohydrodynamic model of Crab nebula radiation." In: 283 (Aug. 1984), pp. 710–730. DOI: 10.1086/162357.

[94] Martı n A. Guerrero et al. "Unveiling shocks in planetary nebulae". In: *Astronomy &amp Astrophysics* 557 (Sept. 2013), A121. DOI: 10.1051/0004-6361/201321786. URL: https://doi.org/10.1051%5C%2F0004-6361%5C%2F201321786.

[95] J S Miller. "Astrophysics of active galaxies and quasi-stellar objects". In: (Jan. 1985). URL: https://www.osti.gov/biblio/5199347.

[96] Maxim Markevitch and Alexey Vikhlinin. "Shocks and cold fronts in galaxy clusters". In: *physrep* 443.1 (May 2007), pp. 1–53. DOI: 10.1016/j.physrep.2007.01.001. arXiv: astro-ph/0701821 [astro-ph].

[97] William John Macquorn Rankine. "XV. On the thermodynamic theory of waves of finite longitudinal disturbance". In: *Philosophical Transactions of the Royal Society of London* 160 (1870), pp. 277–288. DOI: 10.1098/rstl.1870.0015. eprint: https://royalsocietypublishing.org/doi/pdf/10.1098/rstl.1870.0015. URL: https://royalsocietypublishing.org/doi/abs/10.1098/rstl.1870.0015.

[98] ENRICO Fermi. “On the Origin of the Cosmic Radiation”. In: *Phys. Rev.* 75 (8 Apr. 1949), pp. 1169–1174. DOI: 10.1103/PhysRev.75.1169. URL: https://link.aps.org/doi/10.1103/PhysRev.75.1169.

[99] P. D. Hudson. “Reflection of charged particles by plasma shocks”. In: 131 (Jan. 1965), p. 23. DOI: 10.1093/mnras/131.1.23.

[100] Simon F. Portegies Zwart, Stephen L.W. McMillan, and Mark Gieles. “Young Massive Star Clusters”. In: *Annual Review of Astronomy and Astrophysics* 48.1 (Aug. 2010), pp. 431–493. DOI: 10.1146/annurev-astro-081309-130834. URL: https://doi.org/10.1146%2Fannurev-astro-081309-130834.

[101] Bon-Chul Koo and Christopher F. McKee. “Dynamics of Wind Bubbles and Superbubbles. I. Slow Winds and Fast Winds”. In: 388 (Mar. 1992), p. 93. DOI: 10.1086/171132.

[102] Bon-Chul Koo and Christopher F. McKee. “Dynamics of Wind Bubbles and Superbubbles. II. Analytic Theory”. In: 388 (Mar. 1992), p. 103. DOI: 10.1086/171133.

[103] R. Weaver et al. “Interstellar bubbles. II. Structure and evolution.” In: 218 (Dec. 1977), pp. 377–395. DOI: 10.1086/155692.

[104] VS Avedisova. “Formation of Nebulae by Wolf-Rayet Stars.” In: *Soviet Astronomy* 15 (1972), p. 708.

[105] S. R. Kelner, Felex A. Aharonian, and V. V. Bugayov. “Energy spectra of gamma-rays, electrons and neutrinos produced at proton-proton interactions in the very high energy regime”. In: *Phys. Rev. D* 74 (2006). [Erratum: Phys.Rev.D 79, 039901 (2009)], p. 034018. DOI: 10.1103/PhysRevD.74.034018. arXiv: astro-ph/0606058.

[106] P.A. Zyla et al. “Review of Particle Physics”. In: *PTEP* 2020.8 (2020). and 2021 update, p. 083C01. DOI: 10.1093/ptep/ptaa104.

[107] Ivan Esteban et al. “The fate of hints: updated global analysis of three-flavor neutrino oscillations”. In: *Journal of High Energy Physics* 2020.9 (Sept. 2020). DOI: 10.1007/jhep09(2020)178. URL: https://doi.org/10.1007%5C%2Fjhep09%5C%282020%5C%29178.

[108] Paolo Lipari and Silvia Vernetto. “Diffuse Galactic gamma-ray flux at very high energy”. In: *Physical Review D* 98.4 (Aug. 2018). DOI: 10.1103/physrevd.98.043003. URL: https://doi.org/10.1103%2Fphysrevd.98.043003.

[109] M. G. Aartsen et al. “Time-Integrated Neutrino Source Searches with 10 Years of IceCube Data”. In: 124.5, 051103 (Feb. 2020), p. 051103. DOI: 10.1103/PhysRevLett.124.051103. arXiv: 1910.08488 [astro-ph.HE].

[110] A. U. Abeysekara et al. “HAWC observations of the acceleration of very-high-energy cosmic rays in the Cygnus Cocoon”. In: *Nature Astronomy* 5.5 (Mar. 2021), pp. 465–471. DOI: 10.1038/s41550-021-01318-y. URL: https://doi.org/10.1038$%5C%$2Fs41550-021-01318-y.

APPENDIX A: DIFFUSION COEFFICIENT

The expression of the diffusion coefficient of a particle is:

$$D = \frac{1}{3}\frac{R_L v}{\mathcal{F}(k)}, \tag{85}$$

where R_L is the Larmor radius, which allows us to relate the diffusion coefficient with the momentum of a particle; and $\mathcal{F}(k)$ is related to the power spectrum $\mathcal{P}(k)$ of the turbulence on wave number k:

$$\mathcal{F} = \left(\frac{k\mathcal{P}(k)}{B_0^2/8\pi}\right), \tag{86}$$

where $\frac{\mathcal{P}(k)}{B_0^2/8\pi} = \mathcal{P}_0 k^{-\delta}$ with a normalization factor $\mathcal{P}_0$. $\mathcal{P}_0$ is calculated by integrating the region below the power spectra:

$$1 = \int_{k_{min}}^{\infty} \mathcal{P}_0 k^{-\delta} dk. \tag{87}$$

Therefore:

$$\mathcal{P}_0 = (\delta - 1)k_{min}^{\delta-1}, \tag{88}$$

where, k_{min} is the wave number corresponding to the coherence length L_c, which is the largest possible turbulence size of a system. Therefore:

$$L_c = \frac{2\pi}{k_{min}}$$

For resonance scattering under a magnetic field in the system which is purely turbulence, namely $\delta B = B$, the Larmor radius of the particle corresponds to:

$$R_L = \frac{2\pi}{k}$$

Now the diffusion coefficient can be written in terms of Larmor radius and coherence length and index number δ.

$$D = \frac{1}{3}(\delta - 1)cR_L^{1-\delta}L_c^{\delta-1}$$

The factor $(\delta - 1)$ can be ignored due to the uncertainties of R_c and L_c. Then we arrives at the expression:

$$D = \frac{1}{3}cR_L^{1-\delta}L_c^{\delta-1}$$

APPENDIX B: NEUTRINOS AND GAMMA-RAYS FROM P-P INTERACTION

Neutrino

The neutrino model introduced in Kelner et al. (2006) considers two types of neutrino production seperatly: muon neutrino from charged pion decay, and electron neutrino and

muon neutrino from muon decay. The neutrino spectra from charged pion decay($\pi \to \mu\nu_\mu$) is given by:

$$F^{(1)}_{\nu_\mu}(x, E_p) = B' \frac{ln(y)}{y} (\frac{1 - y^{\beta'}}{1 + k' y^{\beta'}(1 - y^{\beta'})})^4 \times [\frac{1}{ln(y)} - \frac{4\beta' y^{\beta'}}{1 - y^{\beta'}} - \frac{4k'\beta' y^{\beta'}(1 - 2y^{\beta'})}{1 + k' y^{\beta'}(1 - y^{\beta'})}]. \tag{89}$$

Here, the x is the ratio of the muon neutrino energy over a specific proton energy $x = E_{\nu_\mu}/E_p$, and $y = x/0.427$. The definition of y makes the spectra have a sharp cutoff at $x = 0.427$. All the other parameters are linked to L, which depends on the proton energy only. L is the natural log of the proton energy normalized to 1 TeV that $L = ln(E_p/1\text{TeV})$. Then we have:

$$B' = 0.175 + 0.204 + 0.010L^2, \tag{90}$$

$$\beta' = \frac{1}{1.67 + 0.111L + 0.0038L^2}, \tag{91}$$

$$k' = 1.07 - 0.086 + 0.002L^2. \tag{92}$$

Eq. (89) gives the scaled spectra of neutrino emission from pion decay at each proton energy. The total neutrino production spectra will be calculated adding over the whole energy range considering the CR spectra and the production rate.

The charged muon subsequently decays and produces two flavors of neutrinos: muon neutrino and electron neutrino. The muon neutrino spectra from muon decay(e.g. $\mu^- \to e^- \nu_\mu \bar{\nu}_e$) is given by:

$$F^{(2)}_{\nu_\mu}(x, E_p) = B_\nu \frac{(1 + k_\nu (lnx)^2)^3}{x(1 + 0.3/x^{\beta_\nu})} (\ln(x))^5. \tag{93}$$

Here, the parameters B_ν, β_ν and k_ν are:

$$B_\nu = \frac{1}{69.5 + 2.65L + 0.3L^2}, \tag{94}$$

$$\beta_\nu = \frac{1}{(0.201 + 0.062 + 0.00042L^2)^{1/4}}, \tag{95}$$

$$k_\nu = \frac{0.279 + 0.141L + 0.0172L^2}{0.3 + (2.3 + L)^2}. \tag{96}$$

The definition of x and L are the same as in the calculation of pion decay neutrino. The electronic neutrino can also be estimated with the same expression:$F_{\nu_e} \approx F^{(2)}_{\nu_\mu}$.

Gamma-ray

The model adopted from Kelner et al. (2006) for gamma-ray spectra from p-p interaction is:

$$F_\gamma(x, E_p) = B_\gamma \frac{d}{dx} [ln(x) (\frac{1 - x^{\beta_\gamma}}{1 + k_\gamma x^{\beta_\gamma}(1 - x^{\beta_\gamma})})^4], \tag{97}$$

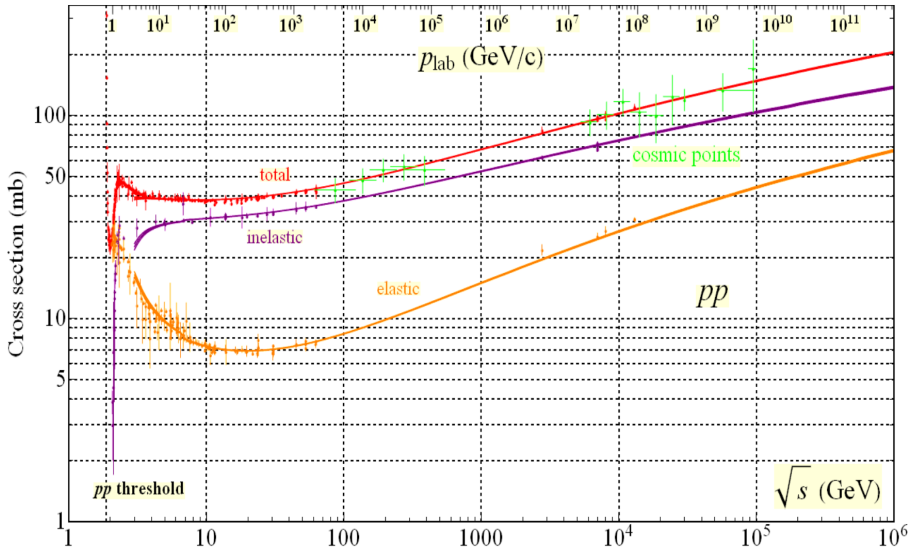

Figure 26: Proton-proton cross section over an energy range from 1 GeV to 1 PeV (Figure by ref [106]).

where x is the ratio of the secondary gamma-ray energy to the primary proton energy x=E_γ / E_p. The parameters B_γ,β_γ and k_γ depend on the proton energy E_p:

$$B_\gamma = 1.30 + 0.14L + 0.011L^2, \tag{98}$$

$$\beta_\gamma = \frac{1}{1.79 + 0.11L + 0.008L^2}, \tag{99}$$

$$k_\gamma = \frac{1}{0.801 + 0.049L + 0.014L^4}. \tag{100}$$

Here, L has the same definition as in the case of neutrinos, so that $L = ln(E_p/1TeV)$. Eq. (97) calculates the scaled spectra of gamma-ray emission at each proton energy. The total gamma-ray production spectra is then calculated considering the CR spectra and the production rate.

APPENDIX C: P-P INTERACTION CROSS SECTION

The lab measured cross section of p-p interaction and its dependence on the proton energy is shown in Fig. 26.